



HAL
open science

Retrieving soil surface roughness with the Hapke photometric model: Confrontation with the ground truth

S. Labarre, S. Jacquemoud, C. Ferrari, A. Delorme, A. Derrien, R. Grandin, M. Jalludin, François Lemaitre, Marianne Métois, Marc Pierrot-Deseilligny, et al.

► To cite this version:

S. Labarre, S. Jacquemoud, C. Ferrari, A. Delorme, A. Derrien, et al.. Retrieving soil surface roughness with the Hapke photometric model: Confrontation with the ground truth. *Remote Sensing of Environment*, 2019, 225, pp.1–15. 10.1016/j.rse.2019.02.014 . hal-02293285

HAL Id: hal-02293285

<https://univ-lyon1.hal.science/hal-02293285>

Submitted on 22 Oct 2021

HAL is a multi-disciplinary open access archive for the deposit and dissemination of scientific research documents, whether they are published or not. The documents may come from teaching and research institutions in France or abroad, or from public or private research centers.

L'archive ouverte pluridisciplinaire **HAL**, est destinée au dépôt et à la diffusion de documents scientifiques de niveau recherche, publiés ou non, émanant des établissements d'enseignement et de recherche français ou étrangers, des laboratoires publics ou privés.



Distributed under a Creative Commons Attribution - NonCommercial 4.0 International License

1 **Date:** Friday, January 25, 2019

2 **Title:** Retrieving soil surface roughness with the Hapke photometric model: confrontation with the
3 ground truth

4 **Authors:** S. Labarre¹, S. Jacquemoud^{1*}, C. Ferrari¹, A. Delorme¹, A. Derrien², R. Grandin¹, M.
5 Jalludin³, F. Lemaître⁴, M. Métois⁵, M. Pierrot-Deseilligny⁶, E. Rupnik⁶, B. Tanguy⁴

6

7 ¹ Institut de physique du globe de Paris - Sorbonne Paris Cité, Université Paris Diderot, UMR CNRS
8 7154, 1 rue Jussieu, 75005 Paris, France (labarre@ipgp.fr; jacquemoud@ipgp.fr; ferrari@ipgp.fr;
9 delorme@ipgp.fr; grandin@ipgp.fr)

10 ² Observatoire Volcanologique du Piton de la Fournaise, Institut de physique du globe de Paris -
11 Sorbonne Paris Cité, Université Paris Diderot, UMR CNRS 7154, 97418 La Plaine des Cafres, La
12 Réunion, France (derrien@ipgp.fr)

13 ³ Centre d'Etude et de Recherche de Djibouti, BP 486, Djibouti, République de Djibouti
14 (mohamed.jalludin@gmail.com)

15 ⁴ ONERA-DOTA - Université de Toulouse, 2 avenue Edouard Belin, BP 74025, 31055 Toulouse
16 Cedex 4, France (francois.lemaitre@onera.fr; bernard.tanguy@onera.fr)

17 ⁵ Laboratoire de Géologie de Lyon - Université Lyon 1, ENS de Lyon, UMR CNRS 5276, 69100
18 Villeurbanne, France (marianne.metois@univ-lyon1.fr)

19 ⁶ Laboratoire en sciences et technologies de l'information géographique - IGN, ENSG, Université
20 Paris-Est, 94160 Saint-Mandé, France (marc.pierrot-deseilligny@ensg.eu;
21 ewelina.rupnik@ensg.eu)

22

23 * Corresponding author

24

25 **Keywords:** very high resolution digital elevation model; surface roughness; multiangular optical
26 remote sensing; field goniometer; Pleiades satellite; Hapke photometric model; Bayesian inversion;
27 Asal-Ghoubbet rift

28

29 **Highlights:**

30

- 31 • Multiangular reflectance and roughness are measured *in situ* on natural soils
- 32 • Multiangular reflectance is determined from Pleiades images
- 33 • A Bayesian inversion of the Hapke model is applied to both datasets
- 34 • Surface roughness retrievals are compared to the ground truth

35

36 **Journal:** *Remote Sensing of Environment*

37

38

39 **Abstract**

40

41 Surface roughness can be defined as the mean slope angle integrated over all scales from the grain
42 size to the local topography. It controls the energy balance of bare soils, in particular the angular
43 distribution of scattered and emitted radiation. This provides clues to understand the intimate structure
44 and evolution of planetary surfaces over ages. In this article we investigate the capacity of the Hapke
45 photometric model, the most widely used in planetary science, to retrieve surface roughness from
46 multiangular reflectance data. Its performance is still a question at issue and we lack validation
47 experiments comparing model retrievals with ground measurements. To address this issue and to

47 show the potentials and limits of the Hapke model, we compare the mean slope angle determined from
48 very high resolution digital elevation models of volcanic and sedimentary terrains sampled in the
49 Asal-Ghoubbet rift (Republic of Djibouti), to the photometric roughness estimated by model inversion
50 on multiangular reflectance data measured on the ground (Chamelon field goniometer) and from space
51 (Pleiades images). The agreement is good on moderately rough surfaces, in the domain of validity of
52 the Hapke model, and poor on others.

53

54 **1. Introduction**

55 Surface roughness, which can be understood as a measure of the topographic relief of a bare soil,
56 plays a key role in micrometeorology, hydrology, volcanology, geomorphology, planetary science and
57 defense among others. It is a multiscale physical parameter which controls the energy balance, the
58 scattering of incident radiation, and the directional emissivity of the ground, opening up the way for
59 understanding its intimate structure and evolution over ages. Multiangular optical imagery is
60 commonly used in planetary science to remotely provide a valuable information about roughness, a
61 physical characteristic of soils that generates shadows at all scales. It is incorporated in photometric
62 models through a shadowing function, with varying complexity. This function can be itself related to
63 different characteristics of the boundary surface: ratio of mean hole depth-to-radius ([Lumme and](#)
64 [Bowell, 1981](#)), mean slope angle of all the facets ([Hapke, 1984](#)), or fractal dimension ([Shkuratov and](#)
65 [Helfenstein, 2001](#)). From a radiometric perspective, the shadowing function partly drives the shape of
66 soil BRF (Bidirectional Reflectance Factor; [Schaeppman-Strub et al., 2006](#)). However, the validation of
67 these models on planetary bodies is indirect.

68 Models using other shadowing functions have been assessed on terrestrial surfaces (e.g.,
69 [Cierniewski, 1987](#); [Irons et al., 1992](#); [Despan et al., 1999](#)) but most of them have been validated only
70 in the lab or in the field. All this work has opened up new perspectives to probe soil physical
71 properties in the solar domain. On Earth, field measurements of surface roughness are pricy, difficult
72 to implement and inefficient to cover large areas. Photogrammetric techniques now provide low-cost
73 high-resolution surface topographic models, from which various statistical parameters can be derived

74 (e.g., [Bretar et al., 2013](#); [Gilliot et al., 2017](#)). Remote sensing allows investigation of large or
75 inaccessible areas. Nonetheless scientists are still looking for a robust method to derive surface
76 roughness. For instance the interpretation of radar images ensuing from the direct link between the
77 backscattering coefficient and roughness remains relatively tricky. LiDAR is also a powerful tool for
78 analyzing soil topography but it is generally limited to the topographic scale.

79 To date the Hapke model is the most widely photometric model used in the scientific community
80 ([Hapke, 2012](#)). Although it gave rise to many improvements over the last thirty years, in particular
81 with regard to the physics of light-matter interaction, its formulation and the significance of its input
82 parameters are still debated. Nevertheless this model is simple and reproduces well the photometric
83 response of bare surfaces measured in the laboratory (e.g., [Jacquemoud et al., 1992](#); [Chappell et al.,](#)
84 [2006](#); [Shepard and Helfenstein, 2007, 2011](#); [Souchon et al., 2011](#); [Beck et al., 2012](#); [Pommerol et al.,](#)
85 [2013](#); [Johnson et al., 2013](#)), in the field (e.g., [Pinty et al., 1989](#); [Johnson et al., 2006a,b](#)) or from space
86 (e.g., [Wu et al., 2009](#); [Ceamanos et al., 2013](#); [Fernando et al., 2013](#); [Vincendon, 2013](#); [Sato et al.,](#)
87 [2014](#)). To what extent multiangular imagery can inform us about soil roughness is, however, still a
88 pending question. The validation of the Hapke model, i.e., the comparison of the retrieved parameters
89 with the ground truth, still requires effort. Multiangular earth-orbiting satellites (e.g., MISR, Pleiades,
90 POLDER, Proba-1, SkySat) are designed to sample the directional reflectance over bare soils at
91 various spatial and spectral resolutions in the visible and near-infrared wavelengths. However, due to
92 the scarcity of concomitant *in situ* surface roughness and radiometric measurements, their ability to
93 retrieve soil roughness has not been demonstrated so far.

94 This article aims at estimating surface roughness on bare soils using the Hapke model from both
95 field and orbital photometric data, and to compare the retrieved values with *in situ* measurements
96 acquired in the Asal-Ghoubbet rift (Republic of Djibouti). First, we present the study site and *in situ*
97 measurements ([section 2](#)). Next, we expose the Pleiades satellite data after atmospheric correction and
98 cross calibration with field data ([section 3](#)). A Bayesian inversion of the Hapke model is performed on
99 both field and satellite data to estimate the photometric roughness of 12 sites and discuss the

100 coherence between the retrieved values (section 4). Finally, a discussion of the results is provided
101 (section 5).

102

103 2. Field data

104 2.1. Study site

105 The Asal-Ghoubbet rift (Republic of Djibouti) is a young active rift. It began to form 900,000 years
106 ago by extending the Somalia-Saudi plate boundary from the oceanic domain towards the west, to the
107 triple point of Africa-Arabia-Somalia, currently located within the depression of Afar. It has been the
108 subject of many research works in geophysics since the early 1970s because it allows small-scale
109 study of the oceanic accretion above sea level (Fig. 1).

110

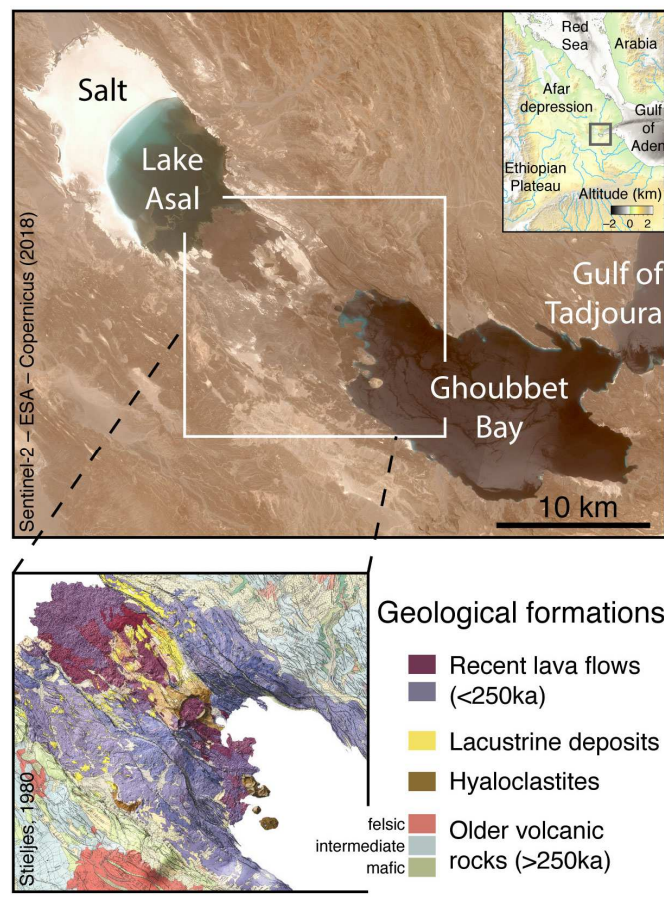


Fig. 1. Geographic context of the study site (11°35'N, 42°29'E). The image on top is a Sentinel-2 image of the Asal-Ghoubbet rift, Djibouti, acquired on 26 May 2018. The main water bodies and recent lava flows can be distinguished by their darker color, whereas recent sedimentary deposits (including salt deposits) have a brighter aspect. The bottom panel is a simplified geological map of the main area of interest targeted in this study (Stieljes, 1980, modified from Pinzuti et al., 2013).

111

112 This unique site meets the objectives of our study for two reasons:

113 1/ it displays a wide variety of bare soils over a small area (~100 km²), from pure white salt
114 deposits to dark lava basalt flows, a contrasted topography, and a great wealth of surfaces, from
115 very rough lava flows to flat deposits in sedimentary basins (Fig. 2);

116 2/ it has a desert climate so that soils are marginally wet and sparsely vegetated. Because of the
117 presence of shoreline terraces generated during the formation of the rift, the lands are generally
118 homogeneous and flat.

119 A first exploratory mission has been conducted in April 2015 to identify areas of interest, and the
120 main campaign took place for two weeks in February 2016. Although organizing a field trip in this rift
121 is a challenge (desert area, strong winds, rudimentary infrastructure), it is easily accessible by car,
122 which makes it an ideal playground for our study.

123



Fig. 2. Twelve surfaces of increasing roughness studied in the Asal-Ghoubbet rift. From top left to bottom right, clay deposits (site F); reshaped hyaloclastic projections (site Y); lapilli deposits (site A); salt bank (site H); centimetric lava blocks (hyaloclastite) on lacustrine deposits (site E); slag on lacustrine deposits (site R); decimetric lava blocs on lacustrine deposits (site I); pulverulent limestone, rich in mollusc shells (site T); altered aphyric lava (site S); cracked lava crust (site M); basalt porphyry lava in the form of slabs (site Q); ropy pahoehoe lava (site B). See [Caminiti \(2000\)](#) for more information about the geomorphology of the rift.

124

2.2. *In situ* roughness measurement

In order to determine the roughness parameter from the slope distribution of these terrains, the topography has been reconstructed at the millimeter scale by means of UAV imaging.

2.2.1. Topographic reconstruction at millimeter scale

Twenty two sites spanning over $30\text{ m} \times 40\text{ m}$ areas have been surveyed using a quadcopter (DJI F450) equipped with a flight control system, a compact-system camera (Sony Alpha 5100) and an interchangeable lens (Sigma 30 mm F2.8). The quadcopter was maintained at a flight altitude between 8 m and 15 m to obtain a pixel size on the ground ranging from 1 to 2 mm. In this windswept region, the camera settings (i.e., exposure time, aperture, and sensitivity) were adapted to each site so as to provide correct image exposure. A camera calibration was also performed in the vicinity of the survey area for maximum precision in the digital elevation model (DEM) reconstruction phase. To realize it, a set of convergent images of a three-dimensional scene (rocks, buildings, etc.) was taken by hand prior to each UAV acquisition.

The quadcopter was flown by an operator along parallel lines above the surface. Flight height and path were controlled by real-time GNSS feedback on the aircraft position. An image overlap of 80% along the flight line and of 50% across the flight line was achieved by controlling the camera automatic shooting time interval, the UAV speed and the trajectory. To geo-reference the images, five ground control points designed to be easily identified in the UAV images were distributed symmetrically across each measured site, and their geographical coordinates were measured with dual-frequency GPS receivers (Ashtech Z-X) and their antennas (Ashtech Geodetic 4) at 1 Hz sampling frequency. The accuracy of the position of these targets was estimated at approximating $1 \pm 0.7\text{ cm}$ (latitude), $0.4 \pm 0.3\text{ cm}$ (longitude) and $1.3 \pm 1.1\text{ cm}$ (altitude). In addition, wooden pieces of defined dimensions ($150\text{ mm} \times 35\text{ mm} \times 35\text{ mm}$) were spread in the fields to provide three-dimensional control information for *a posteriori* DEM validation.

The workflow to reconstruct the high resolution topography follows the steps described by [Bretar et al. \(2013\)](#). It is based on MicMac, an open-source photogrammetric software

152 (<https://micmac.ensg.eu/>) (Pierrot-Deseilligny et al., 2006; Rupnik et al., 2017). About 12 out of 22
153 sites (A, B, E, F, H, I, M, Q, R, S, T and Y) have been processed to date on various reasons including
154 wrong internal calibrations, overlapping problems, and time constraints. The spatial resolution of the
155 DEMs ranges from 2.5 mm to 4 mm. Fig. 3 displays the shaded relief of four contrasted sites
156 presented in Fig. 2. The planimetric accuracy is of the order of a few millimeters, while the relative
157 vertical positional errors on the wooden pieces mentioned above are less than 3%.
158

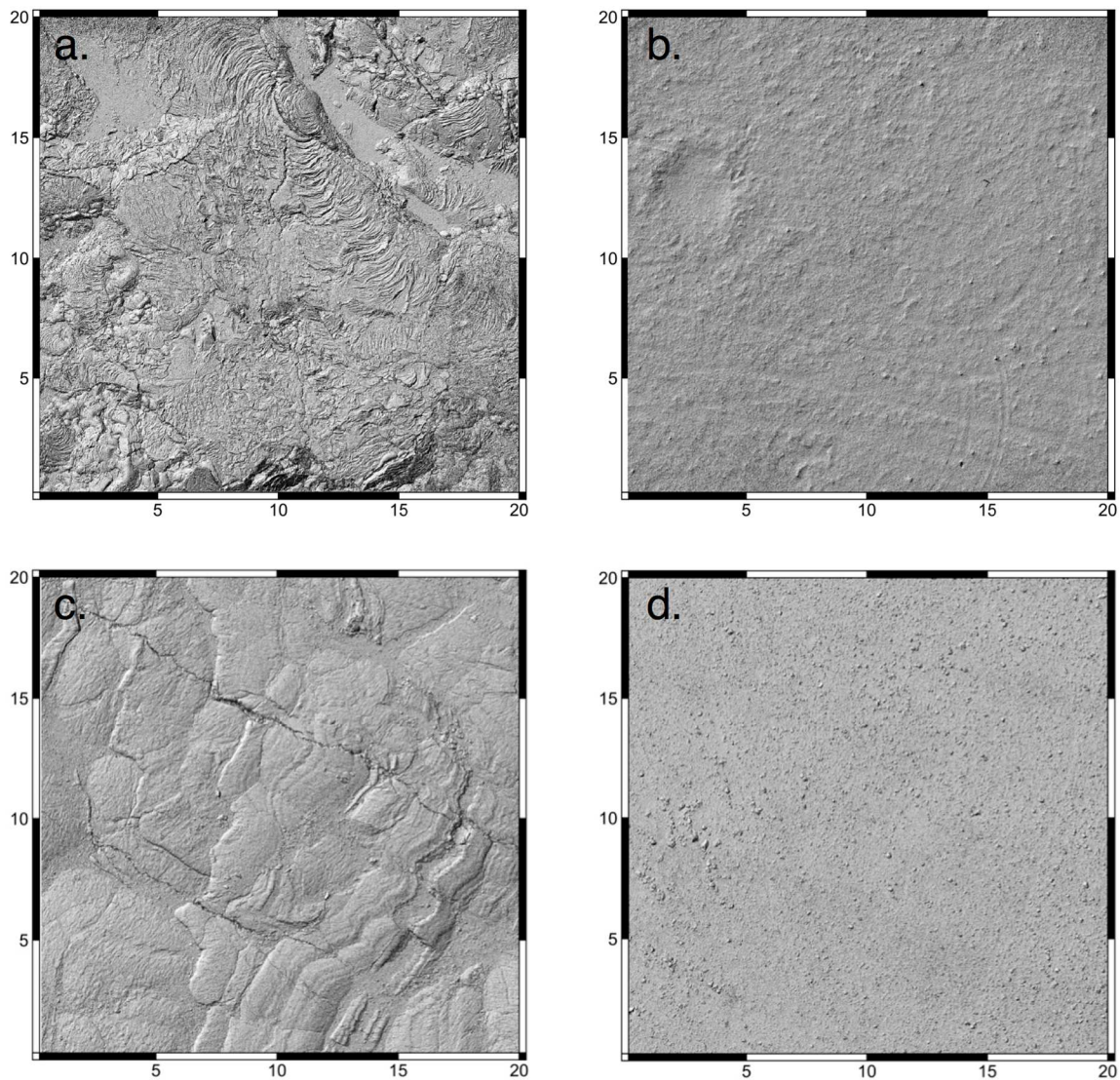


Fig. 3. 20 m long-sided areas extracted from shaded relief maps of digital elevation models for four remarkable sites of the Asal-Ghoubbet rift: sites (a) B, (b) F, (c) M, and (d) R. The spatial resolution of these four DEMs ranges from 2.8 mm to 3.2 mm.

159

160 2.2.2. Surface roughness determination

161 The mean roughness parameter $\bar{\theta}$ was computed using Eq. (1) (Labarre et al., 2017).

$$\tan \bar{\theta} = \frac{2}{\pi} \int_0^{\pi/2} a(\theta) \tan \theta d\theta \quad (1)$$

164 with θ being the slope angle of each facet of the surface and $a(\theta)$ the slope angle distribution. In
 165 order to compare the roughness between sites, a square 20 m on a side was first extracted from each
 166 DEM and then decomposed into twenty-five squares 4 m on a side to facilitate computations. The
 167 mean and the standard deviation of $\bar{\theta}$ calculated for the 12 sites are given in [Table 1](#) and the slope
 168 distributions are illustrated in [Fig. 4](#). The slopes of the two smoothest sites, F and Y, are less than 50°.
 169 Sites E and R show similar distributions. The distribution of site B and site Q reveals very few values
 170 greater than 70° because they present little discontinuities. Sites M and S have the same roughness
 171 and similar distributions, except that the amplitude at angles higher than 50° is stronger for site S due
 172 to the presence of pebbles and centimeter blocks on the surface. The roughness of sites B, A and Y is
 173 comparable to that found in the Piton de La Fournaise for similar terrains ([Bretar et al., 2013](#); [Labarre](#)
 174 [et al., 2017](#)).

Site	Latitude N	Longitude E	Description	$\bar{\theta}$	SD
A	11.5810209904	42.4930719598	Lapilli deposits	18.6	±2.1
B	11.5945984130	42.4726550328	Ropy pahoehoe lava	33.4	±5.1
E	11.5936487248	42.4917893931	Centimetric lava blocks (hyaloclastite) on lacustrine deposits	23.1	±2.9
F	11.5925120813	42.4958721760	Clay deposits	8.3	±1.7
H	11.6199221528	42.3965061773	Salt bank	20.9	±2.2
I	11.5633683315	42.4485707122	Decimetric lava blocs on lacustrine deposits	27.9	±2.4
M	11.5896442760	42.5030110060	Cracked lava crust	18.3	±1.9
Q	11.5618838898	42.5136321246	Basalt porphyry lava in the form of slabs	33.1	±4.2
R	11.5361663318	42.4923411655	Slag on lacustrine deposits	23.1	±1.3
S	11.5416993639	42.4811000172	Altered aphyric lava	18.3	±2.6
T	11.5585832484	42.4558691802	Pulverulent limestone, rich in mollusc shells	20.9	±2.6
Y	11.5864054883	42.4881465853	Reshaped hyaloclastic projections	12.6	±2.0

Table 1. Geographical coordinates, geological description, mean roughness ($\bar{\theta}$) and standard deviation (SD) of 12 sites. The values of $\bar{\theta}$ and SD expressed in degrees are calculated over 25 tiles of 16 m² each.

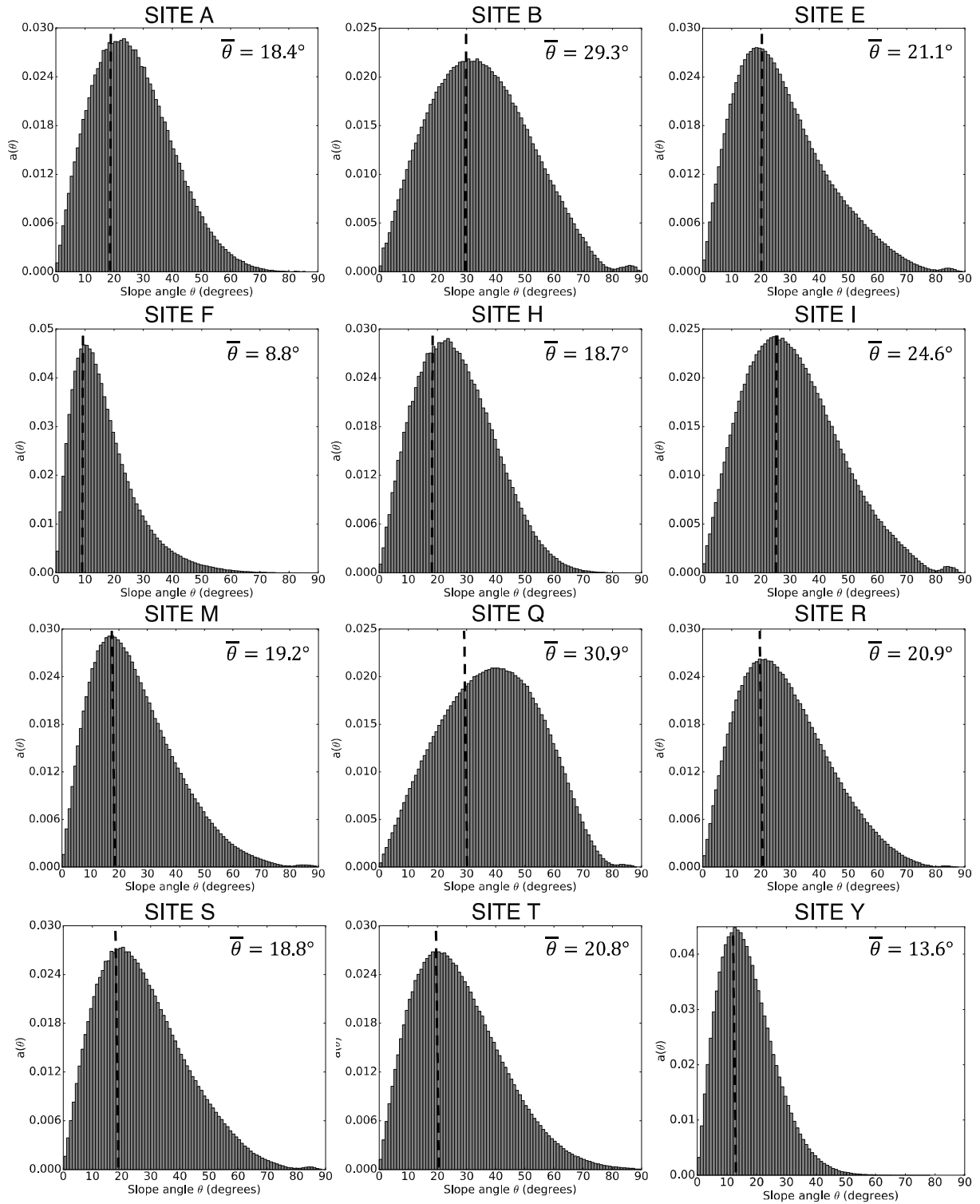


Fig. 4. Slope distribution evaluated on one tile representative of the twelve sites introduced in Fig. 2. The dashed lines correspond to the roughness values $\bar{\theta}$ determined using Eq. 1. Note that the values indicated in each panel are slightly different from those displayed in Table 1, which are averages of 25 tiles.

177

178 **2.3. *In situ* multi-angular photometric measurements**

179 In order to estimate the photometric roughness with the Hapke model at microscopic and
 180 mesoscopic scales, the bidirectional and spectral radiances were measured in the field over 10 of the
 181 selected soils (A, D, E, F, H, M, O, Q, R, and T) with the Chamelon, a new portable field goniometer

182 system designed by ONERA (Toulouse, France) to record the hemispherical conical reflectance factor
183 and coupled with a FieldSpec 4 spectroradiometer (ASD Inc.). They are both remotely controlled by
184 an in-house developed software and mounted on a cart equipped with wheels to facilitate movement.
185 Such outdoor measurements that developed in recent years are still challenging (e.g., [Sandmeier,](#)
186 [2000](#); [Doctor et al., 2015](#); [Bachmann et al., 2016](#); [Furey, 2016](#); [Harms et al., 2016](#)). The remoteness of
187 the Asal-Ghoubbet rift, strong winds and high temperatures during the field experiment made things
188 even more difficult.

189 A four-axis articulated arm allowed to perform directional measurements. The radiance of each
190 targetted field was measured using a fixed 8° instantaneous field-of-view (IFOV): this corresponds to
191 a disk of about 20.56 cm in diameter at nadir, assuming a conical view and a distance to the target of
192 147 cm. This footprint changes to an ellipse with increasing viewing angle: it is four time bigger at a
193 60° viewing angle. The measurements are made according to the following protocol ([Fig. 5](#)): the
194 Chamelon is facing the sun; the solar zenith angle i is calculated knowing the Julian day, the universal
195 time, the latitude and longitude of the site; the articulated arm moves in five measurement planes: two
196 principal planes of the Sun (left and right side), one perpendicular plane, and two 45° planes (left and
197 right side). The radiance of the ground is acquired in thirteen viewing directions e from -59.11° to
198 $+59.09^\circ$ in each of the five planes, and in-between, the radiance of a Spectralon reference panel
199 (Labsphere) is acquired at nadir. At the end of an acquisition cycle, the arm circularly moves around
200 the device to sample the surface at nadir. A complete cycle thus represents 103 measurements: 7
201 vertical measurements on the Spectralon panel, 5×13 directional measurements and $15 + 16$ vertical
202 measurements.

203

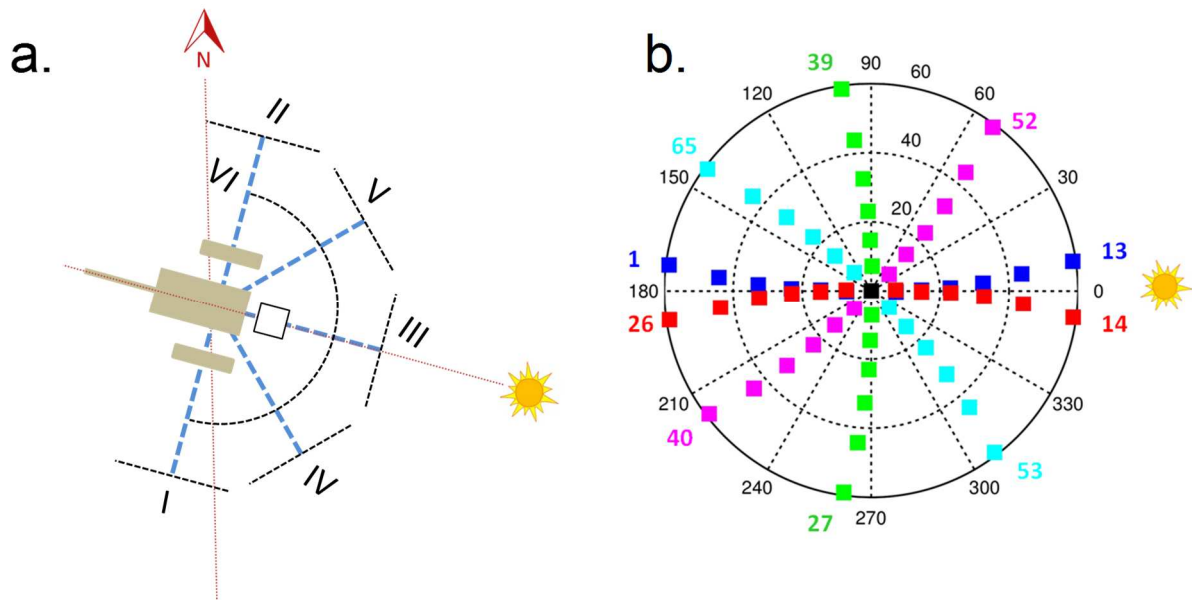


Fig. 5. (a) Measuring planes of the Chamelon field spectro-goniometer: (I) right principal plane of the Sun, (II) left principal plane of the Sun, (III) perpendicular plane, (IV) oblique plane at 45° azimuth on the right, (V) oblique plane at 45° azimuth on the left, and (VI) circular sight. (b) Sampled viewing directions: main plane on the right (blue), main plane on the left (red), perpendicular plane (green), oblique plane at 45° azimuth on the right (magenta), oblique plane at 45° azimuth on the left (cyan). The numbers from 1 to 65 indicate the order of the directional measurements.

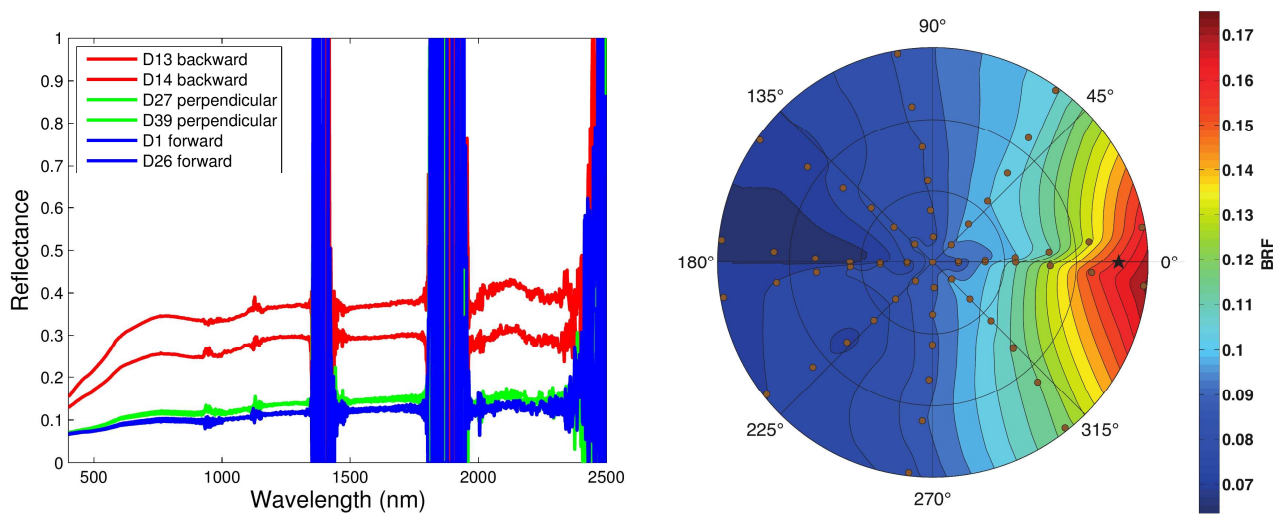
204

205 A cycle approximately lasts 17 min whereas the sun zenith and azimuth angles are likely to vary
 206 from 0.43° to 4.81° and from 0.83° to 9.32°, respectively, depending on the time of the day.
 207 Variations in sun zenith angle are more important early in the morning and late in the afternoon.
 208 Conversely, variations in solar azimuthal angle are maximum around noon. Such variations are not
 209 inconvenient for the inversion of the Hapke model, because the illumination and viewing angles are
 210 exactly known for each measurement.

211 In order to appraise the spatial variability of the bidirectional reflectance factor, between two and
 212 six positions were sampled within each site by moving the Chamelon a few meters. For portability
 213 reasons, and since the size of the smallest area measured on the ground must be statistically
 214 representative of the site, the rougher terrains have not been measured.

215 The radiance of the Spectralon panel measured at close intervals is used to determine the BRF of
 216 the soils, but also to detect instrumental drifts or to remove data affected by clouds. Fig. 6a shows the
 217 reflectance of site A measured between 400 nm and 2500 nm in six viewing directions, symmetrical
 218 with respect to the principal plane of the Sun. Ideally, they should be paired: this is the case in the
 219 directions 1 and 26 (principal planes of the Sun I and II in the forward direction) and in the directions

220 27 and 39 (perpendicular plane III), but not in the directions 13 and 14 (principal planes of the Sun I
 221 and II in the backward direction). The fact that the Chamelon targets different spots during the
 222 acquisition cycle is certainly the cause of the discrepancy that is greater in the backward direction due
 223 to the hotspot effect. Fig. 6b displays the BRF of the same site in the visible. The asymmetry observed
 224 in the hot spot direction is a consequence of the difference of reflectance measured between the
 225 directions 13 and 14.
 226



227 **Fig. 6.** (left) Reflectance spectra of site A for six viewing directions as described in Fig. 5a. The noisy values around 1400
 228 nm, 1900 nm, and 2500 nm are located in spectral regions where atmospheric water vapor strongly absorbs radiation. (right)
 229 Bidirectional reflectance factor of site A averaged over the panchromatic band of Pleiades (see Fig. 7c).

227

228 3. Satellite data

229 The agility of the Pleiades satellite allows unique measurements of the ground BRF at macroscopic
 230 scale. A sensitivity analysis demonstrates the impact of the aerosol optical thickness on the observed
 231 BRF. Cross-calibration with the Chamelon data improves the atmospheric correction by fixing the
 232 other important factor impacting the correction, i.e., the adjacency radius.

233

234 3.1. Pleiades images

235 The Pleiades 1A and 1B satellites, launched in December 2011 and December 2012 respectively,
 236 operate on the same quasi-circular orbit at an altitude of 694 km and they are 180° out of phase. They
 237 aim to image the surface of the Earth in the visible-near infrared wavelengths with both a 50 cm

238 spatial resolution in panchromatic mode and a 2 m spatial resolution in multispectral mode (blue,
 239 green, red, and near infrared) (Fig. 7c). In addition to a high spatial resolution, they offer exceptional
 240 agility that allows rapid off-nadir acquisitions up to $\sim 50^\circ$, thus offering many different observation
 241 geometries (Gleyzes et al., 2012; Lachérade et al., 2012). One can take advantage of this property to
 242 produce high resolution DEMs (Rupnik et al., 2018). During the in-orbit commissioning phase of the
 243 Pleiades 1B satellite conducted by CNES (Centre national d'études spatiales), a series of twenty-one
 244 multiangular images were acquired in video mode in a single flyby of the Asal-Ghoubbet rift on
 245 January 26, 2013 (Figs. 7a,b). The total acquisition time was about four minutes, from 7:49:18 UTC
 246 to 7:53:27 UTC. The swath along the orbital track varied from ~ 20 km at nadir to ~ 60 km at grazing
 247 angle. The high resolution multi-angular reflectances acquired with a large angular sampling over a
 248 wide range of surfaces in terms of color, roughness and mineralogical properties, is unique.
 249

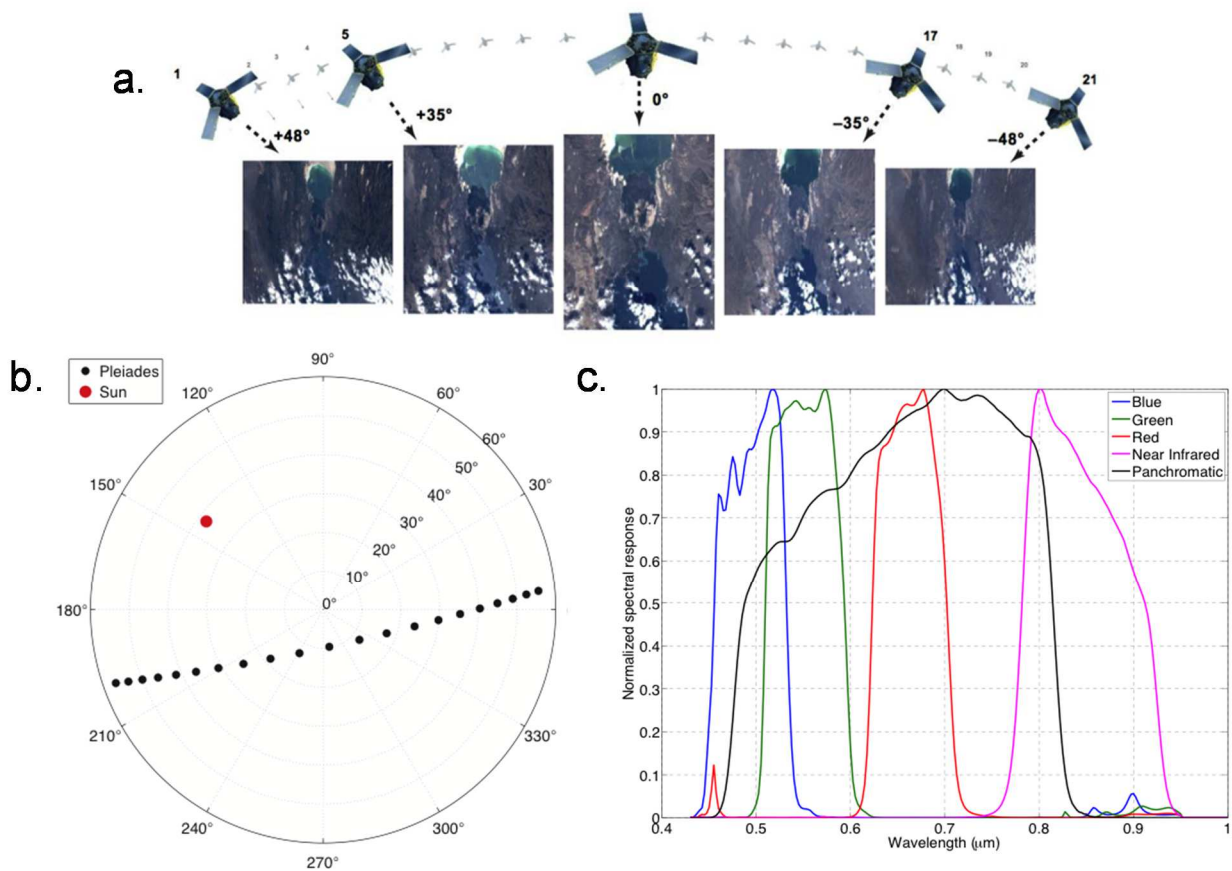


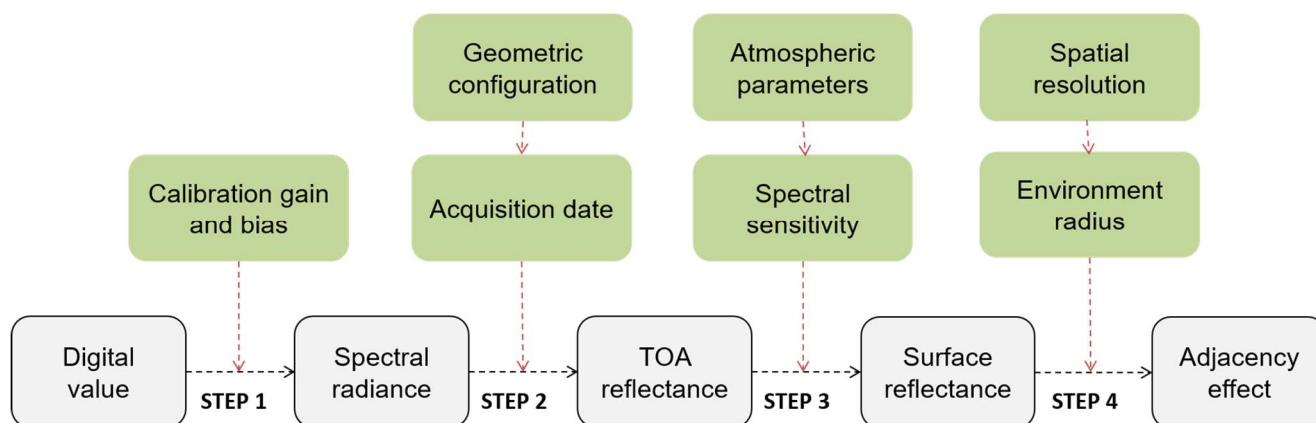
Fig. 7. (a) Visual representation of the Pleiades video acquisition; (b) Observing geometry of the studied zone: the black dots indicate the viewing directions and the red disk the position of the Sun in an azimuth-elevation projection; (c) Normalized spectral bands of the Pleiades satellite (Lachérade et al., 2012).

250

251 3.2. Atmospheric corrections

252 The atmospheric correction of the 21 Pleiades images is a critical step impacting the shape of the
 253 BRF, therefore the accuracy of the retrieved surface roughness. It is based on the 6S radiative transfer
 254 code (Vermote et al., 1997) which is implemented in the Orfeo ToolBox library (OTB,
 255 <https://www.orfeo-toolbox.org/>), a set of algorithmic bricks and satellite image processing utilities
 256 developed by CNES and designed to process the Pleiades images (Fig. 8). Four atmospheric
 257 parameters have to be provided using ancillary datasets: the atmospheric pressure P_a , the water vapor
 258 content U_{H_2O} , the ozone content U_{O_3} , and the aerosol optical thickness τ_A . They were all determined
 259 over Djibouti on January 26, 2013.

260



261 **Fig. 8.** Orfeo ToolBox (OTB) processing chain for radiometric calibration of the Pleiades images. The white frames represent the steps and the green frames the input parameters.

262

263 Atmospheric pressure and ozone content do not vary much spatially and temporally, so they can be
 264 estimated from low spatial resolution meteorological data. On the contrary, water vapor and aerosol
 265 content are highly variable so the calibration requires data with high temporal and spatial resolution.
 266 In the absence of atmospheric measurements as the satellite flew over the Asal-Ghoubbet rift, the
 267 aerosol optical thickness was provided by the MODIS (*Moderate Resolution Imaging Spectrometer*)
 268 instrument onboard the AQUA satellite: $\tau_A = 0.22$. The water vapor content was also derived from the
 269 MODIS instrument onboard the TERRA satellite: $U_{H_2O} = 2.325 \text{ g.cm}^{-2}$. The column ozone content
 270 has been derived from the OMI (*Ozone Monitoring Instrument*) spectrophotometer onboard the
 AURA satellite: $U_{O_3} = 244 \text{ DU}$. Finally, the Global Modeling and Assimilation Office that supports

271 NASA's Earth Science mission uses the GEOS-5 atmospheric data assimilation model to build a
272 consistent temporal database for sea level atmospheric pressure: $P_a = 1014.72$ hPa.

273 The 6S code computes four radiometric quantities in the solar domain between 400 nm and 2500
274 nm: the intrinsic reflectance and the spherical albedo of the atmosphere, the total gaseous
275 transmission, and the total transmittance of the atmosphere along both the sun-surface and surface-
276 satellite optical paths. To take into account the adjacency effect, the average reflectance from
277 contiguous pixels within a circle of radius r around the target pixel is calculated and a correction is
278 made (Appendix A). The processing chain leading to the surface reflectance of the region of interest is
279 applied to the 21 images separately, and the region of interest is then projected onto each sensor
280 geometry as a polygon. The bidirectional reflectance value at a given viewing angle is the mean value
281 of the pixels included in the resulting polygon and the error is the confidence interval at 95%.

282

283 **3.3. Sensitivity of bidirectional reflectance to atmospheric parameters**

284 As mentioned earlier, the shape of the BRF is of critical importance to the retrieval of accurate
285 surface roughnesses. In order to quantify the impact of atmospheric corrections on the calculation of
286 surface reflectance, a one-factor-at-a-time sensitivity analysis of the atmospheric parameters was
287 carried out on two zones selected on criteria of color and roughness (Fig. 9): zone 1 is a silty, flat and
288 bright surface while zone 2 is basalt, rough and dark lava flow. The reflectance factor is first
289 calculated at ground level using the default parameter set implemented in the OTB: $U_{O_3} = 0$ DU,
290 $U_{H_2O} = 2.5$ g. cm⁻², $P_a = 1030$ hPa, $\tau_A = 0.2$, desert aerosol model, and no adjacency effect
291 correction.

292 The effect of water vapor is limited to a modulation of the amplitude of the reflectance. It is
293 reduced in the visible with variations less than 5%, and notable in the near infrared beyond 700 nm
294 due to the presence of weak absorption bands. The ozone content has a larger impact in the visible, in
295 particular in the green band of Pleiades covering the Chappuis band between 550 nm and 650 nm, and
296 has no effect in the near infrared. The influence is important at grazing angles, which results in a
297 significant deformation of the multi-angular reflectance. The atmospheric pressure has a relative

298 impact of less than 5%. Like water vapor, it acts as a scaling factor and is not critical to the correction
299 of the reflectance. Conversely, one can observe a strong influence of aerosol optical thickness on the
300 shape of the reflectance distribution, especially in zone 2 which is darker. The difference with the
301 reference distribution can reach 100% for extreme values, and it tends to increase with the viewing
302 angle or towards shorter wavelengths. Finally, extending the adjacency radius changes both the
303 amplitude and the shape of the reflectance distribution. Therefore, the two most influential
304 atmospheric parameters critical for the determination of soil roughness are the aerosol optical
305 thickness and the adjacency radius.

306

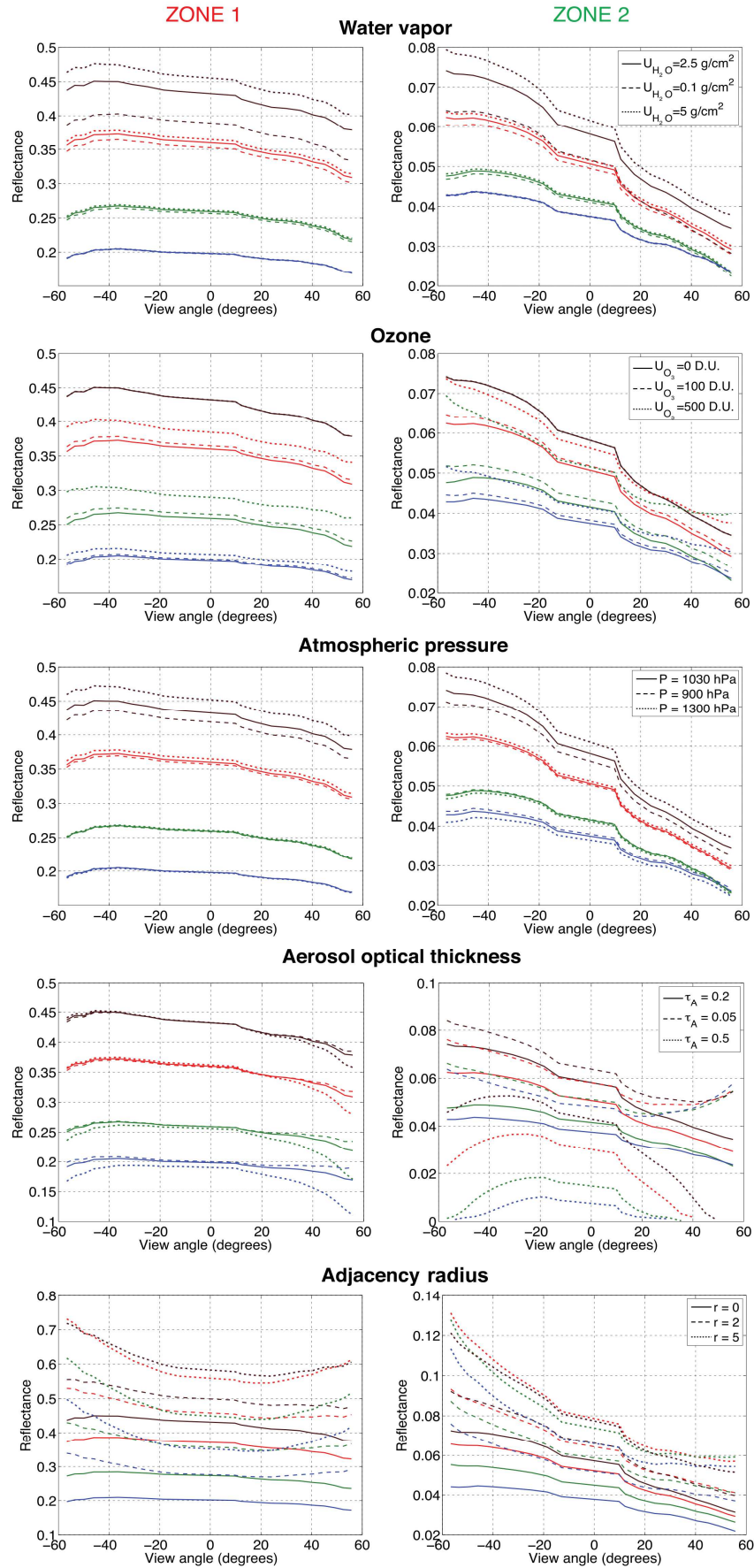


Fig. 9. Determination of the bidirectional reflectance factor (BRF) of two contrasted zones (left/right) in the four Pleiades bands (R: red lines, G: green lines, B: blue lines, PIR: black lines) along the acquisition geometry (Fig. 3) for the default parameters set (solid line) and high (dotted line) and low (dashed line) values of the parameters of the atmospheric correction. The adjacency radius r is expressed in pixel.

307

308 **3.4. Cross-calibration between Pleiades and Chamelon measurements**

309 *In situ* measurements conducted in the Asal-Ghoubbet rift were used as ground truth to check and
 310 to adjust the quality of the orbital measurements. We superimposed the Pleiades reflectances acquired
 311 in four spectral bands and at 21 viewing angles on the Chamelon reflectances acquired from 400 nm
 312 to 900 nm and at 65 viewing angles. **Fig. 10** displays the reflectance factor ratio relative to the green
 313 band, chosen arbitrarily, for sites F (clay deposits), M (decimetric lava blocs on crust), and T
 314 (pulverulent limestone) and two adjacency radii ($r = 0$ and $r = 1$). The agreement is best when $r = 1$
 315 so we used this value to extract the photometric curves of the Pleiades images. On applying this
 316 correction the reflectance as derived from Pleiades tends to decrease in the near infrared down to a
 317 lower value than in the red (**Fig. 10**). This effect is greater for site M, the spectral signature of which is
 318 typical of lunar basalts (e.g., [Staid, 2000](#); [Antonenko and Osinki, 2010](#)).

319

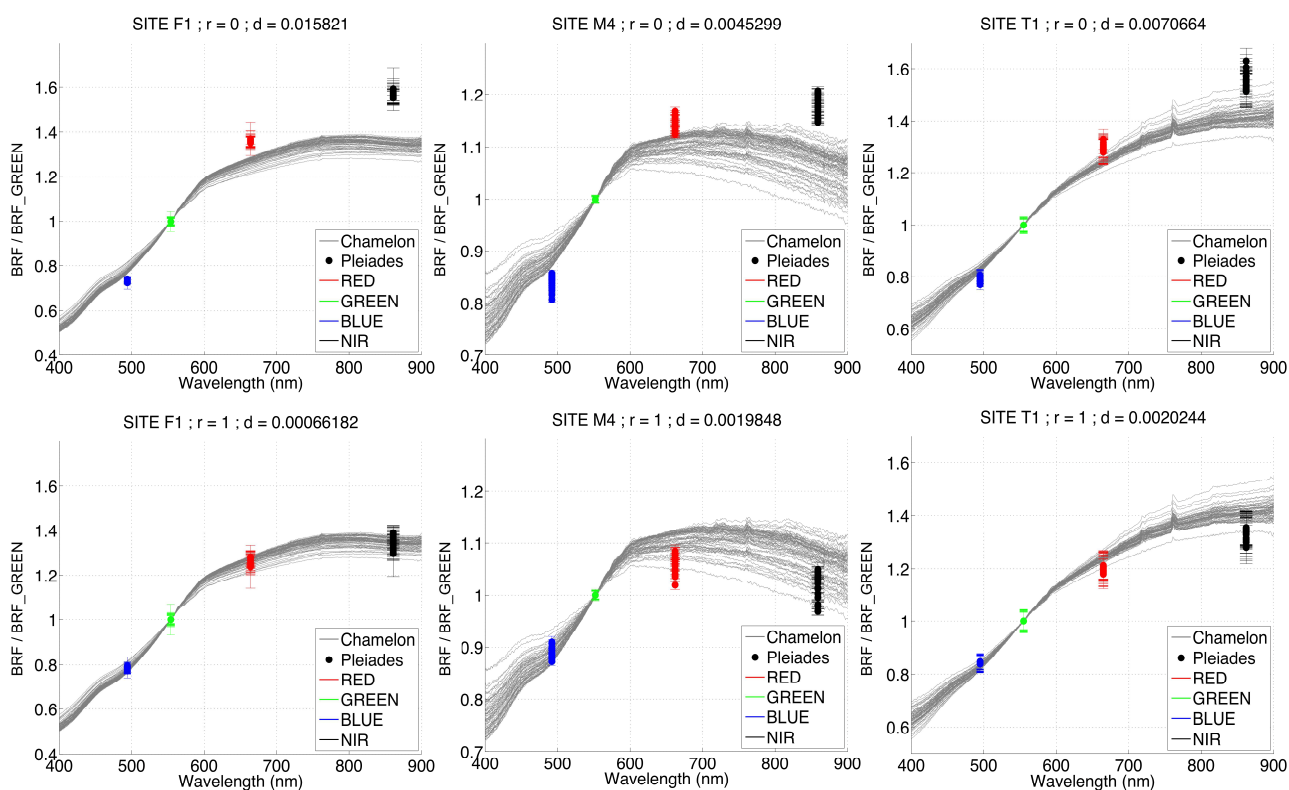


Fig. 10. Comparison between the ratio to the green band of the bidirectional reflectance factor (BRF) spectra for the Chamelon (gray curves) and Pleiades (colored dots) for different values of the adjacency effect radius ($r = 0$ at the top; $r = 1$ at the bottom) and for the sites F (left), M (middle) and T (right) of the Asal-Ghoubbet rift.

320

321 **3.5. Pleiades multiangular reflectance**

322 **Fig. 11** illustrates the bidirectional reflectance factor (BRF) extracted over 12 sites in the four
323 spectral bands of the Pleiades satellite after calibration. The average albedo of sites F (clay deposits),
324 T (pulverulent limestone) and H (salt bank) changes from bright to very bright. The shape of the BRF
325 versus the viewing angle of site H is slightly convex, whereas that of site F is flat and collapses at
326 grazing viewing angles. Site T exhibits a negative slope. The shape and magnitude of the BRF of the
327 other sites are similar in the four spectral bands, except at site R for which some points are missing
328 due to the presence of clouds and shadows, and sites B and Q that display lower amplitude. The BRF
329 of sites A, S and Y is similar despite different surface features. The roughest surfaces of sites B and Q
330 are also comparable. At first glance, one can note that the Pleiades BRF does not vary much in shape
331 and that the albedo seems to be a more robust segmentation criterion.

332

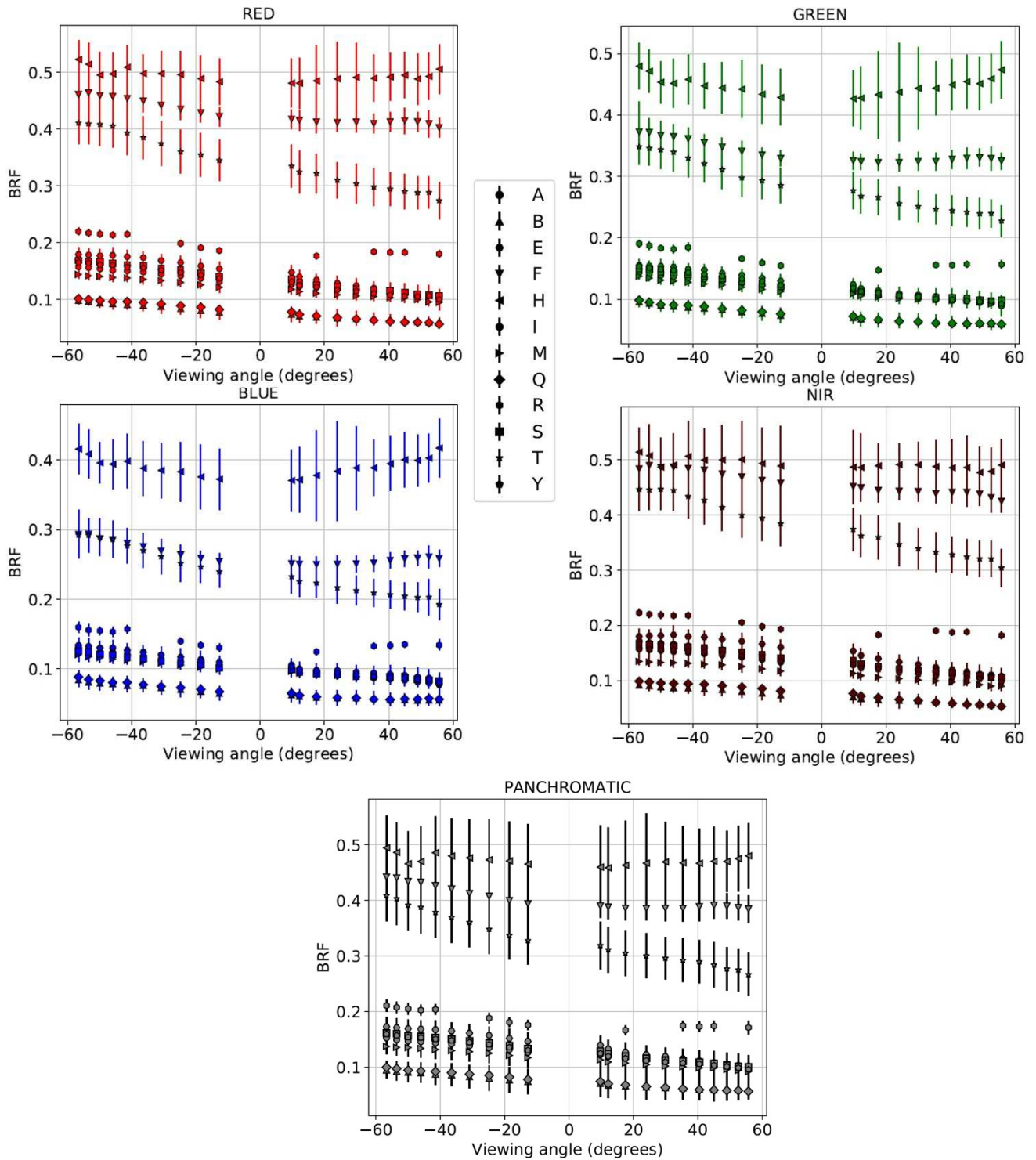


Fig. 11. Bidirectional reflectance factor (BRF) measured by Pleiades at twelve sites of the Asal-Ghoubbet rift in the four spectral bands and the panchromatic band of the sensor. By convention, the negative viewing angles correspond to azimuth angles ranging from 90° to 270° (Fig. 7b).

333

334 **4. Results on soil roughness**

335 In this section we examine whether the mean surface roughness derived from very high resolution
 336 DEMs is consistent with the photometric roughness retrieved by inversion of the Hapke model on soil
 337 multiangular reflectance data acquired at centimeter and meter scales.

338

339 **4.1. The Hapke model**

340 The bidirectional reflectance factor of a particulate medium can be calculated using the radiative
341 transfer model developed by [Hapke \(1981\)](#). The latest version that considers the porosity correction is
342 written as ([Hapke, 2008](#)):

343

$$\pi r_R(i, e, g) = \frac{K(P) w}{\mu_0} \frac{\mu_{0e}}{4 \mu_{0e} + \mu_e} [p(g, b, c) B_S(B_0, P, g) + M(w, \mu_{0e}, \mu_e)] S(i, e, g, \overline{\theta_H}) \quad (2)$$

344

345 with $K(P)$ the porosity coefficient related to the porosity P of the medium, w the single-scattering
346 albedo (ratio of scattering coefficient to total extinction coefficient), i and e the illumination and
347 viewing angles, respectively ($\mu_0 = \cos i$ and $\mu = \cos e$), $p(g, b, c)$ the phase function for the phase
348 angle g and the phase function parameters b (anisotropy parameter) and c (backscattering coefficient),
349 B_S the function describing the shadow-hiding opposition effect (SHOE) and depending on the
350 parameter B_0 , named opposition surge amplitude, M a function modeling multiple scattering, and S a
351 shadowing function quantifying the effects of the photometric roughness $\overline{\theta_H}$ ([Appendix B](#)). μ_{0e} and
352 μ_e are the cosines of the effective illumination and viewing angles, the expressions of which depend
353 on $\overline{\theta_H}$.

354

355 **4.2. Photometric roughness**

356 Many authors have inverted the Hapke model by using conventional non-linear least squares
357 methods but the parameter uncertainties have been seldom, if ever, determined (e.g., [Jacquemoud et](#)
358 [al., 1992](#); [Gunderson et al., 2006](#); [Shepard and Helfenstein, 2007](#); [Wu et al., 2009](#); [Helfenstein and](#)
359 [Shepard, 2011](#)). [Fernando et al. \(2015\)](#) and [Schmidt and Fernando \(2015\)](#) recently demonstrated the
360 relevance of a probabilistic inversion to estimate the photometric parameters of the model over Mars.
361 We followed their approach on the Pleiades and Chamelon reflectances.

362 The complete Hapke model depends on six parameters (w , $\overline{\theta}$, B_0 , P , b and c) for which no prior

363 information is available. A uniform probability density function (PDF) is thus considered over their
364 range of variation. Outside this range, the PDF equals zero to discard nonphysical solutions. A global
365 sensitivity analysis of the model recently performed by [Labarre et al. \(2017\)](#) confirmed that the
366 opposition surge amplitude B_0 did not influence the estimation of the other parameters, which was
367 suspected by other authors (e.g., [Wu et al., 2009](#); [Fernando et al., 2013](#)). However we left it free
368 during the inversion insofar as the calculation time was not significantly affected. The inversion of the
369 model was performed using the Python PyMC library ([Patil, 2010](#)) that implements Bayesian
370 statistical models and fitting algorithms, including Markov Chains Monte Carlo. The retrieved values
371 of the parameters are the median of the *a posteriori* PDF provided by PyMC, and the uncertainties
372 corresponds to the 95% confidence interval. The inversion is a two-stage process: first synthetic tests
373 are carried out in different geometrical configurations; second the model is inverted on the Pleiades
374 and Chamelon data. Only three parameters are likely to be accurately constrained by inversion from
375 the observations: w , $\overline{\theta_H}$ and b .

376 Since the grain size is assumed to be larger than the wavelength (a major hypothesis of the model),
377 the roughness and the phase function parameters are assumed to be wavelength independent. Same
378 with the porosity and the opposition effect parameter, the influence of which on the model is small.
379 Therefore, the single scattering albedo, which is related to the optical constants of the constituting
380 materials of the medium, is the only wavelength-dependent parameter. Because of the interactions
381 between w and some parameters ([Labarre et al., 2017](#)), their estimated values may vary with
382 wavelength, although this is physically meaningless.

383 The inversion of the Hapke model was first conducted both on the spectral (R, G, B and NIR)
384 and the panchromatic (P) bands of Pleiades. In total 21 viewing angles were available for the 12 sites
385 except for site R where the number of observations was reduced to 13 due to the presence of clouds in
386 some images. Although the preliminary tests revealed a deterioration in the estimation of the
387 photometric parameters as the number of observations decreased, the constraint on the parameters
388 remained good on this site. Assuming that only w varies spectrally, we also inverted the model on the
389 four spectral bands simultaneously, as suggested by [Jacquemoud et al. \(1992\)](#), [Chappell et al. \(2006\)](#)

390 and Wu et al. (2009). This led to the retrieval of 9 parameters: the four single scattering albedos (w_R ,
391 w_G , w_B and w_{NIR}), the photometric roughness ($\overline{\theta_H}$), the two phase function parameters (b and c), the
392 porosity (P) and the opposition surge amplitude (B_0). By providing better observational constraints,
393 the quality of the retrieval is generally improved. Without information on the uncertainty associated
394 with the Chamelon observations, we fixed it to 10% of the observed values. Although between two
395 and six complete BRFs are available in each site, we inverted the Hapke model on only one chosen on
396 the basis of the stability of atmospheric conditions, the homogeneity of the surface, and the symmetry
397 of the BRF with respect to the principal plane of the Sun. The Chamelon spectra were convoluted by
398 the filter functions of the Pleiades sensor displayed in Fig. 3c to obtain spectrally homogeneous data.
399 The retrieved values of $\overline{\theta_H}$, the parameter of interest, are gathered in Table 2 and Figure 12. The
400 single scattering albedo w is added to check consistency of the Chamelon-Pleiades cross-calibration.
401

Site	Sensor	Photometric roughness $\overline{\theta_H}$		Single scattering albedo w				
		P	MS	P	B	G	R	NIR
A	Pleiades	21.1 ± 16.1	21.9 ± 3.2	0.34 ± 0.17	0.26 ± 0.09	0.29 ± 0.11	0.33 ± 0.12	0.34 ± 0.12
	Chamelon	25.8 ± 6.8	24.7 ± 3.7	0.33 ± 0.15	0.28 ± 0.10	0.37 ± 0.12	0.37 ± 0.12	0.39 ± 0.12
B	Pleiades	28.5 ± 27.2	19.9 ± 16.2	0.30 ± 0.26	0.22 ± 0.09	0.24 ± 0.10	0.25 ± 0.10	0.24 ± 0.10
E	Pleiades	33.7 ± 23.6	29.2 ± 6.5	0.46 ± 0.29	0.33 ± 0.12	0.38 ± 0.13	0.43 ± 0.14	0.44 ± 0.15
	Chamelon	30.5 ± 7.3	30.7 ± 3.6	0.40 ± 0.18	0.31 ± 0.14	0.35 ± 0.15	0.43 ± 0.17	0.46 ± 0.17
F	Pleiades	24.8 ± 15.8	27.1 ± 5.2	0.86 ± 0.13	0.43 ± 0.69	0.79 ± 0.13	0.88 ± 0.11	0.90 ± 0.09
	Chamelon	19.5 ± 3.4	18.9 ± 2.4	0.93 ± 0.04	0.81 ± 0.04	0.88 ± 0.04	0.94 ± 0.03	0.95 ± 0.02
H	Pleiades	14.8 ± 14.7	22.5 ± 14.5	0.89 ± 0.16	0.86 ± 0.13	0.90 ± 0.11	0.93 ± 0.10	0.93 ± 0.10
	Chamelon	22.2 ± 5.7	21.6 ± 2.7	0.93 ± 0.05	0.88 ± 0.03	0.91 ± 0.03	0.94 ± 0.02	0.96 ± 0.02
I	Pleiades	31.8 ± 22.0	30.6 ± 8.6	0.44 ± 0.28	0.35 ± 0.15	0.39 ± 0.16	0.43 ± 0.17	0.43 ± 0.17
M	Pleiades	32.1 ± 21.6	28.3 ± 4.5	0.40 ± 0.27	0.32 ± 0.12	0.35 ± 0.13	0.37 ± 0.13	0.36 ± 0.13
	Chamelon	40.8 ± 5.0	41.5 ± 3.5	0.28 ± 0.14	0.19 ± 0.06	0.21 ± 0.07	0.23 ± 0.07	0.23 ± 0.07
Q	Pleiades	26.4 ± 25.5	19.0 ± 13.5	0.26 ± 0.25	0.20 ± 0.08	0.22 ± 0.08	0.23 ± 0.09	0.23 ± 0.08
	Chamelon	22.0 ± 7.0	22.0 ± 3.6	0.21 ± 0.09	0.18 ± 0.07	0.19 ± 0.07	0.21 ± 0.08	0.21 ± 0.08
R	Pleiades	24.0 ± 15.7	25.7 ± 3.3	0.53 ± 0.23	0.42 ± 0.14	0.47 ± 0.14	0.54 ± 0.15	0.54 ± 0.15
	Chamelon	25.4 ± 6.30	25.5 ± 3.1	0.45 ± 0.17	0.40 ± 0.10	0.45 ± 0.11	0.51 ± 0.11	0.54 ± 0.12
S	Pleiades	29.4 ± 22.4	24.6 ± 4.9	0.41 ± 0.28	0.28 ± 0.10	0.33 ± 0.11	0.37 ± 0.11	0.36 ± 0.12
T	Pleiades	26.4 ± 20.2	24.3 ± 14.2	0.74 ± 0.25	0.54 ± 0.17	0.61 ± 0.18	0.69 ± 0.18	0.73 ± 0.18
	Chamelon	23.1 ± 5.3	22.1 ± 2.9	0.71 ± 0.18	0.58 ± 0.12	0.64 ± 0.12	0.73 ± 0.12	0.79 ± 0.12
Y	Pleiades	31.4 ± 23.7	24.4 ± 14.2	0.45 ± 0.28	0.32 ± 0.12	0.36 ± 0.14	0.38 ± 0.15	0.37 ± 0.15

Table 2. Single scattering albedo w and photometric roughness $\overline{\theta_H}$ estimated by inversion of the Hapke model on multispectral (MS) and panchromatic (P) data. B, G, R and NIR stand for the blue, green, red and near-infrared bands of Pleiades, respectively.

402
403 On the one hand, the single scattering albedo of these sites covers the entire possible range of
404 variation (from 0.21 to 0.93). The high values ($w > 0.8$) retrieved in sites F and H, the brightest

405 surfaces, are close to values found over snowy surfaces or on icy satellites (Verbiscer et al., 2013).
406 The synthetic tests showed a trend to overestimate this parameter, despite a good constraint brought
407 by the *a posteriori* PDF. It is therefore likely that the true value of w is less than that estimated.
408 However, the relative values are coherent: the sites made of blocks and slabs of basaltic lava flows (B,
409 M, and Q) are the darkest ($w < 0.4$), those made of granular deposits and boulders on sedimentary
410 deposits (A, E, I, R, and S) are moderately bright ($0.4 < w < 0.6$), and those made of clay, salt and
411 limestones (F, H, and T) are the brightest ($w > 0.6$). As for the spectral evolution of w , it agrees with
412 previous studies (e.g., Johnson et al., 2006a,b; Chappell et al., 2009; Wu et al., 2009; Sato et al.,
413 2014). Fig. 12a shows the very good agreement between the single scattering albedo estimated from
414 Pleiades and *in situ* Chamelon instrument. This is not surprising since the geometric correction
415 parameter r has been chosen so as to minimize the residual error between the Chamelon and Pleiades
416 data.

417 On the other hand, the retrieved values of $\overline{\theta_H}$ fluctuate between 15° and 35° . These values do not
418 appear to reflect the relatively wide range and increasing macroscopic roughnesses observed in Fig. 2.
419 For instance, the photometric roughness of site F might be expected much lower than that of site Q,
420 which is not the case. Fig. 12b shows that the photometric roughness derived either from space or *in*
421 *situ* coincides for almost all the sites, except for sites F and M. In the first case, the value estimated
422 from the Pleiades data is larger, and in the second, it is lower. These discrepancies lie in a poor
423 adjustment of the Hapke model illustrated by larger root-mean-square errors for sites F and M than for
424 the other sites.

425

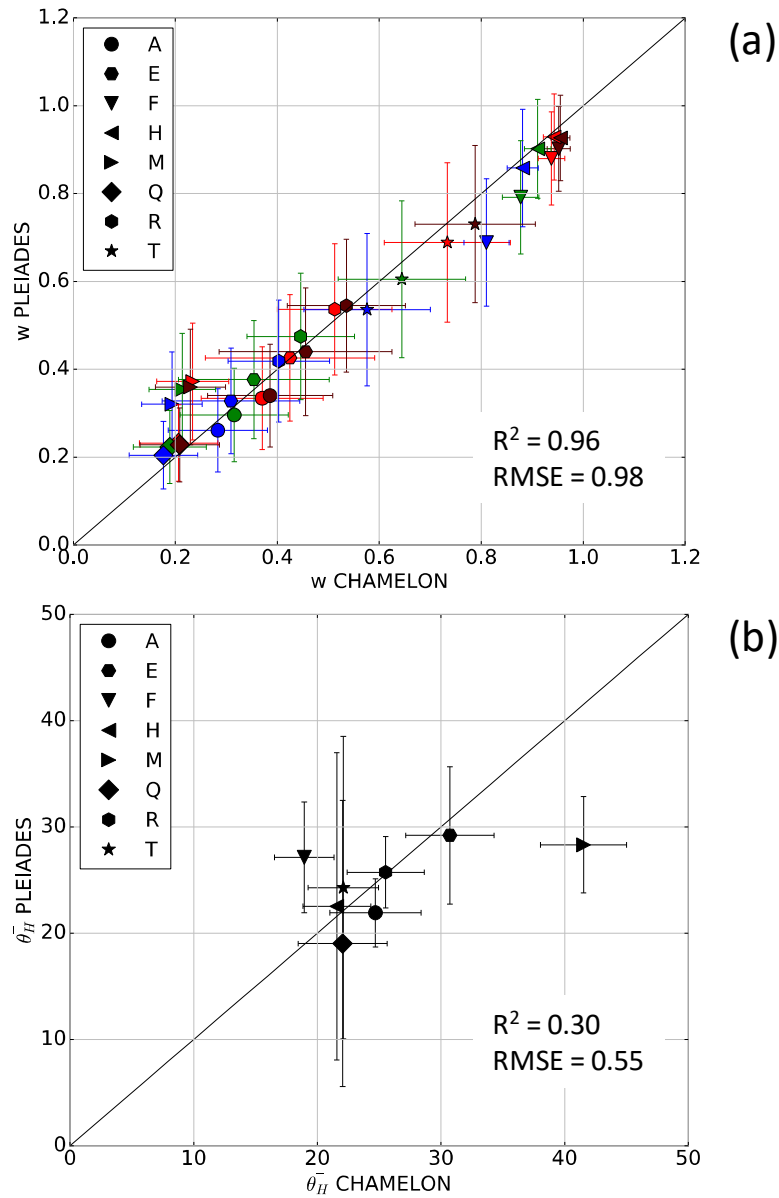


Fig. 12. Comparison of the photometric parameters estimated by Bayesian inversion of the Hapke model on the Pleiades and Chamelon data. (a) Single scattering albedo (blue, green, red and violet colors represent the four Pleiades spectral bands) and (b) Photometric roughness.

426

427 5. Discussion

428 The equivalence between the photometric roughness $\overline{\theta}_H$ estimated by inversion of the Hapke model
 429 and the mean roughness $\overline{\theta}$ measured in the field is not straightforward (Tables 1 and 2, Fig. 13). The
 430 former integrates all scales from the sub-millimeter scale to the decimeter scale, while the latter is
 431 derived from the slope distribution at the smallest DEM scale (~ 3 mm), assumed to be Gaussian. In
 432 most cases, the error bars are compatible with the hypothesis that $\overline{\theta}_H = \overline{\theta}$. Among the sites providing
 433 an error lower than 25%, one can differentiate three groups:

- 434 • Sites A and S that are smooth surfaces consisting of centimetric grains, with similar mean
435 roughness ($\bar{\theta} = 18.57^\circ$ for site A and $\bar{\theta} = 18.31^\circ$ for site S). The uncertainty on $\bar{\theta}_H$ is less
436 than 16%.
- 437 • Sites E, I, R, and T that are made of centimetric to decimetric blocks. The *a posteriori* error on
438 the photometric roughness is more significant, but the correspondence is very good for sites I,
439 R and T. Sites E and R have a very close spatial structure (slag deposits on lacustrine
440 sediments, [Fig. 2](#)) leading to similar $\bar{\theta}$ values. However, the difference between $\bar{\theta}_H$ and $\bar{\theta}$ for
441 site E is slightly larger.
- 442 • Site H that corresponds to the salt lake with a granular structure and optical properties
443 deviating from those of rocky terrain. The uncertainty on the $\bar{\theta}_H$ estimate is very large.

444 The retrieval is poor for sites B (ropy pahoehoe lava), Q (basalt porphyry lava), F (clay deposits),
445 Y (hyaloclastic projections) and M (cracked lava crust). The estimated photometric roughnesses is
446 similar for sites B and Q that are comparable in terms of visual aspect of surface roughness. As far as
447 the Chamelon is concerned, the photometric roughness and the mean roughness measured in the field
448 agree well for moderate roughness (sites A, E, H, R, and T) with a relative error of 17.2%. The
449 absence of correlation for sites F, M and Q still comes out.

450 The sources of discrepancy are difficult to identify. The Orfeo ToolBox used for the atmospheric
451 correction, assumes that the surface is Lambertian, which is naturally wrong in nature and may affect
452 the calculation of the reflectance (e.g., [Lyasputin, 1999](#); [Li et al., 2010](#); [Ceamanos et al., 2013](#)). The
453 effect of the local topography can be also accounted for but we ignored it here because the surfaces
454 studied are nearly flat. [Li et al. \(2012\)](#) highlighted the effectiveness of these two corrections on
455 Landsat temporal data. Therefore, it is likely that an approximate atmospheric correction based on
456 Lambertian assumptions has an impact on the estimation of surface roughness, especially at grazing
457 viewing angles.

458 The estimation of surface roughness through photometric roughness seems to be satisfactory on
459 surfaces displaying granular structures, the size of which is greater than a centimeter, or small blocks.

460 In the case of finer-grained surfaces or more complex structures (slabs, fractures, depressions), the
461 Hapke model fits the observations but the roughness estimates are biased. The performance of the
462 inversion may be poor if the surface departs too much from the hypotheses of the Hapke model.
463 Moreover, the photometric roughness that measures shading at the particle scale is supposed to also
464 depend on the transparency of the particles and their scattering behavior (e.g., [Shepard and Campbell,](#)
465 [1998](#); [Cord et al., 2003](#); [Pilorget et al., 2016](#)). Finally, the Hapke model considers a collimated
466 incident light while the atmospheric scattering makes the sun light a spread source for terrestrial
467 surfaces. This tends to reduce the shadowing on the surface and to underestimate the photometric
468 roughness. Note that the part of the reflectance due to diffuse light is still a pending question on soils,
469 while it has been quantified for a long time on vegetation. Last but not least, [Labarre et al. \(2017\)](#)
470 showed that the photometric roughness was controlled by the smallest scales of the surface. Thus, it is
471 likely that this parameter is sensitive to scales smaller than the scale of the DEMs produced in this
472 study for the computation of the mean roughness parameter. This would result in an underestimation
473 of $\bar{\theta}$, in particular for the smoothest surfaces.

474

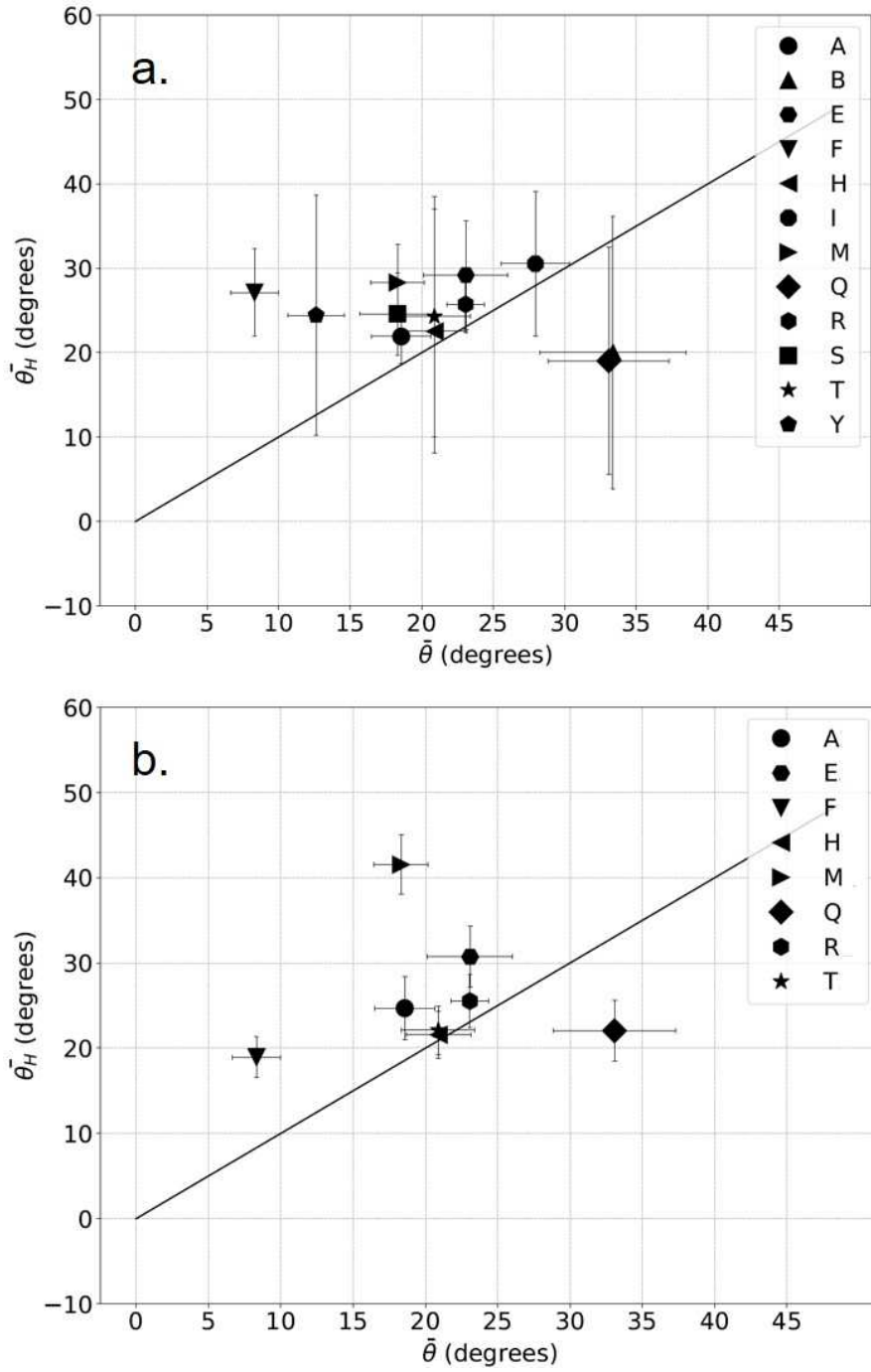


Fig. 13. Estimated photometric roughness $\bar{\theta}_H$ as a function of the measured mean roughness $\bar{\theta}$ for 12 sites (see Fig. 2) from (a) Pleiades data and (b) Chamelon data.

475

476 6. Conclusion

477 We have investigated the capacity of the Hapke model to retrieve the surface roughness of bare
 478 soils from multiangular reflectance data. This model is indeed commonly used in planetary science
 479 even if its validation is still an open issue. We aimed at coupling *in situ* measurements on bare soils
 480 with remote multiangular observations at high resolution to address this issue or show the potentials
 481 and limits of these data and method. Because of its agility and spatial resolution, the Pleiades satellite

482 was able to measure angular reflectance of natural surfaces of reduced extend and wide diversity,
483 from space, from a large number of viewing angles, which, with a few exceptions is unique on Earth
484 remote sensing. If performant this model would provide a new physical description of bare soils with
485 many derived applications.

486 For the first time we measured the topography of large areas ($\sim 20 \text{ m} \times 20 \text{ m}$) at the millimeter
487 scale, determined their surface roughness defined as the mean slope angle, and tried to relate the
488 photometric roughness as derived from to multi-angular optical data acquired in the field of from
489 space. We showed that the atmospheric correction is critical to estimate surface roughness, due to the
490 strong influence of aerosols but also of the adjacency effect on the shape and amplitude of the
491 bidirectional reflectance. Part of this issue was solved by cross-calibrating remote and *in situ*
492 observations in R,G B and IR bands. We emphasized that the Lambertian assumption enclosed in the
493 software used for the atmospheric correction may have an impact on the results. A Bayesian inversion
494 of the Hapke model was conducted to cope with the non-linearity of the model and to assess the
495 uncertainties associated with parameter estimation. Two approaches were explored: the first one
496 consisting of a simultaneous inversion on the four Pleiades bands, assuming that the single scattering
497 albedo is the only wavelength-dependent parameter, and the second one consisting of an inversion on
498 the panchromatic band. Results were found better in the first case, with greatly reduced uncertainties
499 on the parameters, because of better observational constraints.

500 This study revealed that the coherence between the photometric roughness $\overline{\theta}_H$ and the mean
501 roughness $\overline{\theta}$ was good for moderately rough surfaces presenting homogeneous granular structures, but
502 poor for solid floor areas or highly rough surfaces presenting more complex structures (slabs, hollows,
503 fractures), which do not fit Hapke model hypotheses. This article is the result of an exploratory work
504 and provides a framework to scientists wishing to estimate surface roughness using optical remote
505 sensing. Other experiments will be required at different scales, including the topographic one, before
506 we totally understand the determinism of soil bidirectional reflectance.

507

508 **Acknowledgments**

509 The PhD thesis of Sébastien Labarre was funded by the Direction Générale de l'Armement (DGA)
510 and by the Commissariat à l'Energie Atomique et aux Energies Alternatives (CEA). Field data were
511 acquired in the frame of the CAROLInA (*Characterization of Multi-Scale Roughness using Optical*
512 *ImAgery*) project funded by CNES. The authors would like to thank Sophie Lachérade (CNES) and
513 Claire Tinel (CNES) who enabled us to acquire the Pleiades images, Jean-Bernard de Chabaliér
514 (IPGP) who guided part of the team in the Asal-Ghoubbet rift during the exploratory mission in April
515 2015, H el ene Robic (IPGP), Michel Diament (IPGP) and Yann Klinger (IGGP) for their invaluable
516 help, the CERD team who provided us logistical assistance on the ground. Fig. 1 contains modified
517 Copernicus Sentinel data 2018, processed by ESA.

518

519 **Appendix A. Calibration and atmospheric corrections**

520

521 The calibration and atmospheric correction of the Pleiades images follow the four steps illustrated
522 in Fig. 8. First the numerical value X_k recorded in band k is converted to spectral radiance
523 [$W \cdot m^{-2} \cdot sr^{-1} \cdot \mu m^{-1}$] according to

524

$$I_{k,TOA} = \frac{X_k}{\alpha_k} + \beta_k \quad (A1)$$

525

526 where $I_{k,TOA}$ is the radiance measured at the top of the atmosphere, α_k is the absolute calibration gain,
527 and β_k is the absolute calibration bias. These two parameters are contained in the metadata. The
528 radiance value can be then converted into a TOA reflectance factor:

529

$$\rho_{k,TOA} = \frac{\pi I_{k,TOA} d_0^2}{J_{k,i} \mu_0} \quad (A2)$$

530

531 with $J_{k,i}$ the solar illumination at the upper limit of the atmosphere for the Earth-Sun distance d_0
532 expressed in astronomical units, at the date of acquisition. In order to calculate the surface reflectance,

533 one needs to provide the atmospheric pressure P_a [hPa], the water vapor content U_{H_2O} [$g \cdot cm^{-2}$], the
 534 ozone content U_{O_3} [DU], the aerosol optical thickness τ_A at 550 nm, a predefined aerosol model
 535 (desert) to determine the aerosol phase function P_A and the single scattering albedo ω_0 , as well as
 536 sensor intrinsic parameters (solar and viewing zenith and azimuth angles, acquisition date, sensor
 537 spectral response at a given wavelength).

538 Gases and aerosols are the two major atmospheric constituents causing the extinction of solar
 539 radiation by absorption or scattering. According to Vermote et al. (1997), the TOA reflectance factor
 540 of a uniform and Lambertian surface illuminated with an incidence angle i and observed at a viewing
 541 angle e , is written as

$$542 \quad \rho_{TOA} = \rho_{atm} + T(i)T(e) \frac{\rho_t}{1 - \rho_t S} \quad (A3)$$

543
 544 with ρ_{atm} the intrinsic atmospheric reflectance factor, $T(i)$ and $T(e)$ the total atmospheric
 545 transmittances in the illumination (i) and viewing (e) directions, ρ_t the reflectance factor of the
 546 target, and S the atmospheric spherical albedo. Taking explicitly into account absorption by water
 547 vapor and ozone, the TOA reflectance factor ρ_{TOA} at a given wavelength becomes:

$$548 \quad \begin{aligned} \rho_{TOA}(i, e, \phi, P_a, \tau_A, \omega_0, P_A, U_{H_2O}, U_{O_3}) \\ = T(i, e, \phi, P_a, U_{O_3}) \left[\rho_{atm}(i, e, \phi, P_a, \tau_A, \omega_0, P_A, U_{H_2O}) \right. \\ \left. + T_{atm}(i, e, \phi, P_a, \tau_A, \omega_0, P_A) \frac{\rho_t}{1 - \rho_t S(P_a, \tau_A, \omega_0, P_A)} T_{H_2O}(i, e, U_{H_2O}) \right] \end{aligned} \quad (A4)$$

549
 550 with U_{H_2O} the total atmospheric water vapor content [$g \cdot cm^{-2}$], U_{O_3} the total column ozone content
 551 [DU], T_{H_2O} the transmittance of atmospheric water vapor, T the transmittance of all other gases, T_{atm}
 552 the total atmospheric transmittance, $\phi = \phi_e - \phi_i$ the relative azimuth angle, P_a the atmospheric
 553 pressure [hPa], τ_A the aerosol optical thickness, ω_0 the aerosol single scattering albedo, and P_A the
 554 aerosol phase function.

555 To take into account the nonuniformity of the surface, the average reflectance $\langle \rho \rangle$ of the pixels
 556 surrounding the target pixel is computed as (Vermote et al., 1997):

557

$$\langle \rho \rangle = \int_0^{2\pi} \int_0^\infty \rho'(r, \psi) F(r) d\psi dr \quad (\text{A5})$$

558

559 with $F(r)$ the environmental function (probability that a photon incident on the target be scattered and
 560 impacts the surface within a circle of radius r around the target center) and $\rho'(r, \psi)$ the surface
 561 reflectance in polar coordinates. The boundary conditions are $F(0) = 0$ and $F(\infty) = 1$. $F(r)$ is a
 562 complex function of the molecule and aerosol phase function, their optical thickness and vertical
 563 distribution. Their contribution can be taken into account separately:

564

$$F(r) = \frac{t_d^R(e) F_R(r) + t_d^A(e) F_A(r)}{t_d(e)} \quad (\text{A6})$$

565

566 with $t_d^R(\mu)$ and $t_d^A(\mu)$ the diffuse transmission factors for molecules and aerosols. Finally, the surface
 567 reflectance ρ_c is expressed as

568

$$\rho_c = \frac{\rho_t T(e) - \langle \rho \rangle t_d(e)}{e^{-\tau/\mu}} \quad (\text{A7})$$

569

570 where $t_d(e)$ is the diffuse transmittance factor in the viewing direction, τ is the atmospheric optical
 571 thickness and $\mu = \cos e$.

572

573 **Appendix B. Shadowing function**

574

575 The shadowing function used in Eq. (2) is detailed in Hapke (2012). There are two different ways
 576 of calculating it:

577

$$S(i, e, g, \overline{\theta}_H)_{i \leq e} = \frac{\mu_e \mu_0}{\eta(e) \eta(i)} \frac{\chi(\overline{\theta}_H)}{1 - f(\phi) + f(\phi) \chi(\overline{\theta}_H) [\mu_0 / \eta(i)]} \quad (\text{B1})$$

$$S(i, e, g, \overline{\theta}_H)_{i > e} = \frac{\mu_e \mu_0}{\eta(e) \eta(i)} \frac{\chi(\overline{\theta}_H)}{1 - f(\phi) + f(\phi) \chi(\overline{\theta}_H) [\mu / \eta(e)]} \quad (\text{B2})$$

578

579 with i and e are the illumination and viewing angles, $\overline{\theta}_H$ is the photometric roughness, $\mu_0 = \cos i$,

580 $\mu = \cos e$, and μ_e is the cosine of the effective viewing angle. The functions χ , η and f are written as

581

$$\chi(\overline{\theta}_H) = \frac{1}{1 + \pi \tan^2(\overline{\theta}_H)} \quad (\text{B3})$$

$$\eta(x) = \chi(\overline{\theta}_H) \left[\cos(x) + \sin(x) \tan(\overline{\theta}_H) \frac{E_2(x)}{2 - E_1(x)} \right] \quad (\text{B4})$$

$$f(\phi) = \exp\left(-2 \tan\left(\frac{\phi}{2}\right)\right) \quad (\text{B5})$$

582

583 with

584

$$E_1(x) = \exp\left(-\frac{2}{\pi} \cot(\overline{\theta}_H) \cot(x)\right) \quad (\text{B6})$$

$$E_2(x) = \exp\left(-\frac{1}{\pi} \cot^2(\overline{\theta}_H) \cot^2(x)\right) \quad (\text{B7})$$

585

586 References

- 587 Antonenko I. and Osinki G.R. (2010), Automated detection of basalt spectra in Clementine Lunar data, In *Proc.*
588 *41st Lunar and Planetary Science Conference*, pp. 26–27.
- 589 Bachmann C.M., Abelev A., Montes M.J., Philpot W., Gray D., Doctor K.Z., Fusina R.A., Mattis G., Chen W.,
590 Noble S.D., Coburn C., Corl T., Slomer L., Nichols C.R., van Roggen E., Hughes R.J., Carr S., Kharabash
591 S., Brady A. and Vermillion M. (2016), Flexible field goniometer system: the Goniometer for Outdoor
592 Portable Hyperspectral Earth Reflectance, *Journal of Applied Remote Sensing*, 10(3):036012.
- 593 Beck P., Pommerol A., Thomas N., Schmitt B., Moynier F. and Barrat J.A. (2012), Photometry of meteorites,
594 *Icarus*, 218(1):364–377.
- 595 Bretar F., Arab-Sedze M., Champion J., Pierrot-Deseilligny M., Heggy E. and Jacquemoud S. (2013), An
596 advanced photogrammetric method to measure surface roughness: application to volcanic terrains in the
597 Piton de la Fournaise, Reunion Island, *Remote Sensing of Environment*, 135:1–11.
- 598 Caminiti A.M. (2000), *Le fossé d'Asal et le lac Abhé. Deux sites géologiques exceptionnels en République de*
599 *Djibouti*, Editions Couleur Locale, 128 pp.
- 600 Chappell A., Zobeck T.M. and Brunner G. (2006), Using bi-directional soil spectral reflectance to model soil
601 surface changes induced by rainfall and wind-tunnel abrasion, *Remote Sensing of Environment*, 102(3–
602 4):328–343.
- 603 Chappell A., Leys J.F., McTainsh G.H., Strong C. and Zobeck T.M. (2009), Simulating Multi-angle Imaging
604 Spectro-Radiometer (MISR) sampling and retrieval of soil surface roughness and composition changes
605 using a bi-directional soil spectral reflectance model, in *Recent Advances in Remote Sensing and*
606 *Geoinformation Processing for Land Degradation Assessment* (Roeder A. & Hill J., eds), Taylor &
607 Francis, pp.243–259.
- 608 Cierniewski J. (1987), A model for soil surface roughness influence on the spectral response of bare soil in the
609 visible and near-infrared range, *Remote Sensing of Environment*, 23(1):97–115.
- 610 Cord A., Pinet P., Daydou Y. and Chevrel S. (2003), Planetary regolith surface analogs: optimized

- determination of Hapke parameters using multi-angular spectro-imaging laboratory data, *Icarus*, 165(2), pp.414–427.
- Despan D., Bedidi A. and Cerville B. (1999), Bidirectional reflectance of rough bare soil surfaces, *Geophysical Research Letters*, 26(17):2777–2780.
- Doctor K.Z., Bachmann C.M., Gray D.J., Montes M.J. and Fusina R.A. (2015), Wavelength dependence of the bidirectional reflectance distribution function (BRDF) of beach sands, *Applied Optics*, 54(31):F243.
- Fernando J., Schmidt F., Pilorget C., Pinet P., Ceamanos X., Douté S., Daydou Y. and Costard F. (2015), Characterization and mapping of surface physical properties of Mars from CRISM multi-angular data: application to Gusev Crater and Meridiani Planum, *Icarus*, 253:271–295.
- Furey J. (2016), Laboratory goniometer approach for spectral polarimetric directionality, In *Proc. Polarization: Measurement, Analysis, and Remote Sensing XII* (Chenault D.B. & Goldstein D.H., eds), Baltimore, MD, USA, 17 April 2016, SPIE, Vol. 9853, pp. 98530I.
- Gleyzes M.A., Perret L. and Kubik P. (2012), Pleiades system architecture and main performances, in *International Archives of the Photogrammetry, Remote Sensing and Spatial Information Sciences, XXII ISPRS Congress*, 25 August - 01 September 2012, Melbourne, Australia, Vol. XXXIX-B1, pp. 537–542.
- Gunderson K., Thomas N. and Whitby J.A. (2006), First measurements with the Physikalisches Institut Radiometric Experiment (PHIRE), *Planetary and Space Science*, 54(11):1046–1056.
- Hapke B. (1981), Bidirectional reflectance spectroscopy: 1. Theory, *Journal of Geophysical Research: Solid Earth*, 86(B4):3039–3054.
- Hapke B. (1984), Bidirectional reflectance spectroscopy: 3. Correction for macroscopic roughness, *Icarus*, 59(1):41–59.
- Hapke B. (2008), Bidirectional reflectance spectroscopy: 6. Effects of porosity, *Icarus*, 195(2):918–926.
- Hapke B. (2012), *Theory of Reflectance and Emittance Spectroscopy*, Cambridge University Press, 528 pages.
- Harms J.D., Bachmann C.M., Faulring J.W. and Ruiz Torres A.J. (2016), A next generation field-portable goniometer system. In *Proc. Algorithms and Technologies for Multispectral, Hyperspectral, and Ultraspectral Imagery XXII* (Velez-Reyes M. & Messinger D.W., eds), Baltimore, MD, USA, 17 April 2016, SPIE, Vol. 9840, pp. 98400J.
- Helfenstein P. and Shepard M.K. (1999), Submillimeter-scale topography of the Lunar regolith, *Icarus*, 141(1):107–131.
- Helfenstein P. and Shepard M.K. (2011), Testing the Hapke photometric model: improved inversion and the porosity correction, *Icarus*, 215(1):83–100.
- Irons J.R., Campbell G.S., Norman J.M., Graham D.W. and Kovalick W.M. (1992), Prediction and measurement of soil bidirectional reflectance, *IEEE Transactions on Geoscience and Remote Sensing*, 30(2):249–260.
- Jacquemoud S., Baret F. and Hanocq J.F. (1992), Modeling spectral and bidirectional soil reflectance, *Remote Sensing of Environment*, 41(2–3):123–132.
- Johnson J.R., Grundy W.M., Lemmon M.T., Bell J.F., Johnson M.J., Deen R., Arvidson R.E., Farrand W.H., Guinness E.A., Hayes A.G., Herkenhoff K.E., Seelos F., Soderblom J. and Squyres S. (2006a), Spectrophotometric properties of materials observed by Pancam on the Mars Exploration Rovers: 1. Spirit, *Journal of Geophysical Research: Planets*, 111(E2):E02S14.
- Johnson J.R., Grundy W.M., Lemmon M.T., Bell J.F., Johnson M.J., Deen R., Arvidson R.E., Farrand W.H., Guinness E.A., Hayes A.G., Herkenhoff K.E., Seelos F., Soderblom J. and Squyres S. (2006b), Spectrophotometric properties of materials observed by Pancam on the Mars Exploration Rovers: 2. Opportunity, *Journal of Geophysical Research: Planets*, 111(E12):E12S16.
- Johnson J.R., Shepard M.K., Grundy W.M., Paige D.A. and Foote E.J. (2013), Spectrogoniometry and modeling of martian and lunar analog samples and Apollo soils, *Icarus*, 223(1):383–406.
- Labarre S., Ferrari C. and Jacquemoud S. (2017), Surface roughness retrieval by inversion of the Hapke model: a multiscale approach, *Icarus*, 290:63–80.
- Lachérade S., Fourest S., Gamet P. and Lebègue L. (2012), Pleiades absolute calibration: inflight calibration sites and methodology, in *ISPRS International Archives of the Photogrammetry, Remote Sensing and Spatial Information Sciences, XXXIX-B1*, pp.549–554.
- Li F., Lymburner L., Mueller N., Tan P., Islam A., Jupp D.L.B. and Reddy S. (2010), An evaluation of the use of atmospheric and BRDF correction to standardize Landsat data, *IEEE Journal of Selected Topics in Applied Earth Observations and Remote Sensing*, 3(3):257–270.
- Li F., Jupp D.L.B., Thankappan M., Lymburner L., Mueller N., Lewis A. and Held A. (2012), A physics-based atmospheric and BRDF correction for Landsat data over mountainous terrain, *Remote Sensing of Environment*, 124:756–770.
- Lumme K. and Bowell E. (1981), Radiative transfer in the surfaces of atmosphereless bodies. I. Theory,

- 669 *Astronomical Journal*, 86(11):1694-1721.
- 670 Lyasputin A.I. (1999). Atmospheric and geometrical effects on land surface albedo, *Journal of Geophysical*
- 671 *Research: Atmospheres*, 104(D4):4127–4143.
- 672 McGuire A.F. and Hapke B.W. (1995), An experimental study of light scattering by large irregular particles,
- 673 *Icarus*, 113(1):134-155.
- 674 Patil A. (2010), PyMC: Bayesian stochastic modelling in Python, *Journal of Statistical Software*, 35(4):1–81.
- 675 Pierrot-Deseilligny M. and Paparoditis N. (2006), A multiresolution and optimization-based image matching
- 676 approach: an application to surface reconstruction from SPOT5-HRS stereo imagery, In Proc.
- 677 *Topographic Mapping from Space (with Special Emphasis on Small Satellites)*, 14-16 February 2006,
- 678 Ankara, Turkey, ISPRS Archives, Vol. XXXVI-1/W41, 5 pp.
- 679 Pilorget C., Fernando J., Ehlmann B.L., Schmidt F. and Hiroi T. (2016), Wavelength dependence of scattering
- 680 properties in the VIS-NIR and links with grain-scale physical and compositional properties, *Icarus*,
- 681 267:296–314.
- 682 Pinty B., Verstraete M.M. and Dickinson R.E. (1989), A physical model for predicting bidirectional
- 683 reflectances over bare soil, *Remote Sensing of Environment*, 27(3):273–288.
- 684 Pinzuti P., Humler E., Manighetti I. and Gaudemer Y. (2013), Petrological constraints on melt generation
- 685 beneath the Asal Rift (Djibouti) using quaternary basalts, *Geochemistry, Geophysics, Geosystems*,
- 686 14(8):2932–2953.
- 687 Pommerol A., Thomas N., Jost B., Beck P., Okubo C. and McEwen A.S. (2013), Photometric properties of
- 688 Mars soils analogs, *Journal of Geophysical Research: Planets*, 118(10):2045–2072.
- 689 Rupnik E., Daakir M. and Pierrot-Deseilligny M. (2017), MicMac – a free, open-source solution for
- 690 photogrammetry, *Open Geospatial Data, Software and Standards*, 2:14.
- 691 Rupnik E., Pierrot-Deseilligny M. and Delorme A. (2018), 3D reconstruction from multi-view VHR-satellite
- 692 images in MicMac, *ISPRS Journal of Photogrammetry and Remote Sensing*, 139:201–211.
- 693 Sandmeier S.R. (2000), Acquisition of bidirectional reflectance factor data with field goniometers, *Remote*
- 694 *Sensing of Environment*, 73(3):257–269.
- 695 Sato H., Robinson M.S., Hapke B., Denevi B.W. and Boyd A.K. (2014), Resolved Hapke parameter maps of
- 696 the Moon, *Journal of Geophysical Research: Planets*, 119(8):1775–1805.
- 697 Schaepman-Strub G., Schaepman M.E., Painter T.H., Dangel S. and Martonchik J.V. (2006), Reflectance
- 698 quantities in optical remote sensing—definitions and case studies, *Remote Sensing of Environment*,
- 699 103(1):27-42.
- 700 Schmidt F. and Fernando J. (2015), Realistic uncertainties on Hapke model parameters from photometric
- 701 measurement, *Icarus*, 260:73–93.
- 702 Shepard M.K. and Campbell B.A. (1998), Shadows on a planetary surface and implications for photometric
- 703 roughness, *Icarus*, 134(2):279–291.
- 704 Shepard M.K. and Helfenstein P. (2007), A test of the Hapke photometric model, *Journal of Geophysical*
- 705 *Research: Planets*, 112(E3):E03001.
- 706 Shepard M.K. and Helfenstein P. (2011), A laboratory study of the bidirectional reflectance from particulate
- 707 samples, *Icarus*, 215(2):526–533.
- 708 Shkuratov Y., Starukhina L., Hoffmann H. and Arnold G. (1999), A model of spectral albedo of particulate
- 709 surfaces: implications for optical properties of the Moon, *Icarus*, 137:235–246.
- 710 Shkuratov Y. and Helfenstein P. (2001), The opposition effect and the quasi-fractal structure of regolith: I.
- 711 Theory, *Icarus*, 152(1):96–116.
- 712 Souchon A.L., Pinet P.C., Chevrel S.D., Daydou Y.H., Baratoux D., Kurita K., Shepard M.K. and Helfenstein
- 713 P. (2011), An experimental study of Hapke’s modeling of natural granular surface samples, *Icarus*,
- 714 215(1):313–331.
- 715 Staid M. (2000), Integrated spectral analysis of Mare soils and craters: applications to eastern nearside basalts,
- 716 *Icarus*, 145(1):122–139.
- 717 Stieltjes L. (1980), Carte géologique du rift d’Asal 1/50 000 (Dépression Afar, est-africain. République de
- 718 Djibouti), CNRS Editions, Paris.
- 719 Verbiscer A.J., Helfenstein P. and Buratti B.J. (2013), Photometric properties of Solar System ices, in *The*
- 720 *Science of Solar System Ices* (Gudipati M.S. & Castillo-Rogez J., eds), Springer, pp.47–72.
- 721 Vermote E., Tanré D., Deuzé J.L., Herman M. and Morcrette J.J. (1997), Second Simulation of the satellite
- 722 signal in the solar spectrum (6S): an overview, *IEEE Transactions on Geoscience and Remote Sensing*,
- 723 35:675–686.
- 724 Vincendon M. (2013), Mars surface phase function constrained by orbital observations, *Planetary and Space*
- 725 *Science*, 76(1):87–95.
- 726 Wu Y., Gong P., Liu Q. and Chappell A. (2009), Retrieving photometric properties of desert surfaces in China

